

General Disclaimer

One or more of the Following Statements may affect this Document

- This document has been reproduced from the best copy furnished by the organizational source. It is being released in the interest of making available as much information as possible.
- This document may contain data, which exceeds the sheet parameters. It was furnished in this condition by the organizational source and is the best copy available.
- This document may contain tone-on-tone or color graphs, charts and/or pictures, which have been reproduced in black and white.
- This document is paginated as submitted by the original source.
- Portions of this document are not fully legible due to the historical nature of some of the material. However, it is the best reproduction available from the original submission.



CENTER FOR RADAR ASTRONOMY

STANFORD UNIVERSITY
DEPARTMENT OF ELECTRICAL ENGINEERING
STANFORD, CALIFORNIA 94305

September 13, 1983

Henry C. Brinton
Code EL-4
NASA Headquarters
Washington, DC 20546

Dear Henry:

The five attachments to this letter constitute the final report on PIDP contract NAGW-326, on "Continued Development of the Radio Science technique as a Tool for Planetary and Solar System Exploration".

Attachment A introduces a possible alternative to a spacecraft monostatic radar system for surface studies of Titan. We believe that the potential of the uplink bistatic radar approach is so high that a detailed study should be conducted. We may propose such a study if there is a continuation of the PIDP program in 1984.

Attachment B outlines the results of a short study of the characteristics of a bistatic radar investigation of Titan's surface, presented in terms of the Voyager 1 flyby and a proposed Galileo orbiter of Saturn. It shows the limitations of the downlink bistatic approach and points the way to the need for an uplink experiment of greatly improved sensitivity.

Attachment C is a general outline of the critical factors which need to be addressed in order to optimize the radio occultation technique for the study of clouds and cloud regions in planetary atmospheres.

Attachment D addresses potential improvements in the techniques for measuring small-scale structures in planetary atmospheres and ionospheres. The recent identification (Hinson and Tyler: 1983, Icarus, 54, 337) of the major role of internal gravity waves in Titan's atmosphere represents an important new departure in the general subject of small atmospheric structure, and the method used in isolating and identifying the gravity wave effects need to be perfected and applied to other atmospheres.

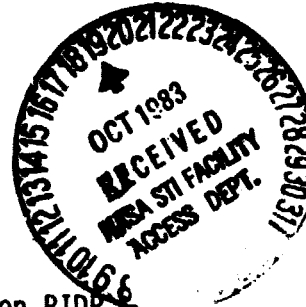
Attachment E is a draft report on the development of a technique for vastly improving the radial resolution from the radio occultation measurements of the rings of Saturn. While this work was supported primarily from other sources, the report is included here because extensions of this technique may well be applicable to obtaining increased height resolution in planetary atmospheres as measured by radio occultation, and improved areal resolution in planetary surface studies by the bistatic radar method. In all cases, the improvements would be due to, and would require, high levels of phase stability, as is demonstrated here from the use of the Voyager USO (ultra-stable oscillator) for the occultation studies of Saturn's rings. It is commonly said that the resolution is set by the size of the principal Fresnel zone, but in the examples here, resolutions to less than a hundredth of the Fresnel zone is achieved in the rings.

(NASA-CR-17 072) CONTINUED DEVELOPMENT OF
THE RADIO SCIENCE TECHNIQUE AS A TOOL FOR
PLANETARY AND SOLAR SYSTEM EXPLORATION
Final Report (Stanford Univ.) 77 p
HC A05/MF A 1

N83-37035

Unclass

CSSL 03A G3/89 15148



September 13, 1983

We believe that important progress has been made during the past year, based on the PIDP support. However, this is a continuing process. We suggest that follow-on efforts are needed in order to optimize the scientific potential of the radio systems that are continuing to be developed for spacecraft telemetry and tracking.

Very truly yours,

A handwritten signature in cursive script, reading "Von Eshleman".

Von R. Eshleman

63:Brinton3
VRE:sz



CENTER FOR RADAR ASTRONOMY

STANFORD UNIVERSITY

DEPARTMENT OF ELECTRICAL ENGINEERING
STANFORD, CALIFORNIA 94305

September 7, 1983

To: Titan-ites (CaTiSiO_5)

From: Von R. Eshleman and G. Leonard Tyler, STAR LAB,
Stanford University, Stanford, California 94305

Re: Uplink Bistatic Radar for Titan Surface Studies

It is generally agreed that the next spacecraft mission to the Saturn system should attempt radar measurements of Titan's surface. Preliminary studies by European and U.S. investigators have included consideration of a spacecraft monostatic radar, such as the Pioneer-Venus Orbiter radar. A group at Stanford University is preparing a proposal to NASA for a detailed study of an alternate radar method, as outlined below. This memo is being sent to interested parties for their information relative to continuing planning of potential missions to the Saturn system.

We suggest consideration of uplink bistatic radar for detection and study of Titan's surface. While most bistatic radar and occultation investigations have been downlink (transmission from spacecraft and reception on Earth), it is important here to realize the factor of 10^3 to 10^4 improvement in sensitivity that should be realized with an uplink experiment using ground-based transmissions and spacecraft receivers. The "science instrument" would be based on the use of the facilities of the NASA-JPL Deep Space Network (in particular, the large ground-based antennas and powerful command transmitters), the spacecraft telemetry antenna and feeds, and part of the spacecraft receivers. Provision of a low noise input stage and a wide-band amplifier chain would be required on the spacecraft, with associated equipment for sampling and storage of data and for merging into the standard data stream. For the surface studies, the spacecraft high-gain telemetry antenna would be pointed toward Titan for the carom signals, but the direct signals would also be received, for reference, through the antenna sidelobes (or through a low-gain antenna, if one were already supplied for the telemetry system). That is, the only equipment supplied specifically for the experiment would be for amplifying, storing, and merging the wide-band bistatic radar data obtained by using the uplink command system.

The Voyager radio-science experimenters considered downlink bistatic radar for Titan surface studies, but did not attempt it because even simple detection of a bounce signal appeared to be unlikely, and because it would have complicated spacecraft operations at a very critical time. However, the proposed uplink experiment would have orders-of-magnitude more sensitivity, so that it might well be capable of obtaining many of the Titan objectives of a spacecraft monostatic radar experiment similar to that of the Pioneer Venus Orbiter. Assuming a Saturn orbiter with repeated Titan encounters, as in the European Cassini study, the bistatic radar studies could include measurements of surface elevations (topography) along different tracks for each encounter, reflection coefficient and Brewster angle measurements to determine the dielectric constant of the surface material, spectral studies to investigate small-scale surface roughness along the radar tracks, and some degree of surface imaging based on time delay and spectral measurements.

While it is clear that a monostatic spacecraft radar system could provide very significant data on Titan's surface, we believe that the uplink bistatic possibility should also be considered and investigated in detail, in case later study of trade-offs might make it a contender.

If the uplink approach were chosen, the same system could be used for detailed investigation of Saturn's rings by the occultation technique, and repeated occultation measurements of the Titan and Saturn atmospheres, at even greater sensitivity and resolution than was obtained in the downlink Voyager experiments. That is, there would be continuing science to be conducted even if Titan's surface turns out to be everywhere the same; i.e., oceanic.

VRS/GLT

Radar Scattering from Titan's Surface Using a Saturn Galileo Spacecraft

Properties of a signal scattered from the surface of Titan during the Voyager I encounter were studied previously. Although some marginal detections appeared possible, no experiment was conducted.

For Voyager, the most likely detection would have occurred when the specular point velocity matched the body rotation - a sort of resonant condition. Even so, the signal had to be observed in a sub-Hertz bandwidth for several minutes before one could expect a detection.

Similar calculations have been performed for a possible Saturn Galileo encounter with Titan. In fact, two cases have actually been considered - one using a spacecraft on a "polar tour" of the Saturnian system and one using an equatorial tour. Results for these, as well as the early Voyager study, are attached.

The polar tour shows the least promise. Though closest approach is after occultation and total echo strength is highest then, so is the bandwidth. Detectability - expressed as strength per unit bandwidth - is never larger than -45dB.

For the Galileo equatorial tour there is a grazing (perhaps atmospheric) occultation about 25 minutes after closest approach. Again, however, maximum strength and maximum bandwidth occur simultaneously. The bandwidth is never less than 20 Hz for this trajectory so there is no possibility of a "resonance" detection. The best detectability for the equatorial tour is about -44dB, shortly after closest approach but before deepest atmospheric penetration.

The radio wavelength assumed for these calculations was 13 cm. Presumably use of 3.6 cm would offer higher transmit/receive antenna gains but with some additional loss to atmospheric absorption and (probably) a higher diffuse-to-specular scatter ratio. Highest detectabilities were obtained for grazing incidences, so these factors would have to be considered more carefully before any decisions were made.

The surface of Titan was assumed to be perfectly reflecting with 6°rms (gently undulating) roughness. Lower reflectivity - which would be expected for a dielectric - would degrade the detectability. Increased roughness - such as is found on the outer three Galilean satellites - would also reduce chances for detection. On the other hand, Mars - another body with an atmosphere - appears to have only 2°rms roughness (and sometimes less) on its north polar cap.

The "resonance" detection is very sensitive to Titan's pole vector and rotation rate - which, for this study were assumed to be perpendicular to its orbital plane and synchronous, respectively. The Galileo trajectory is sufficiently oblique to Titan's equatorial plane that no resonance condition was found.

To get the most out of a Titan BSR encounter, two conditions must be changed:

- a) The trajectory must be closer to Titan equatorial, and
- b) The encounter velocity must be reduced

Given a detectable signal the following (partially dependent) parameters could be estimated:

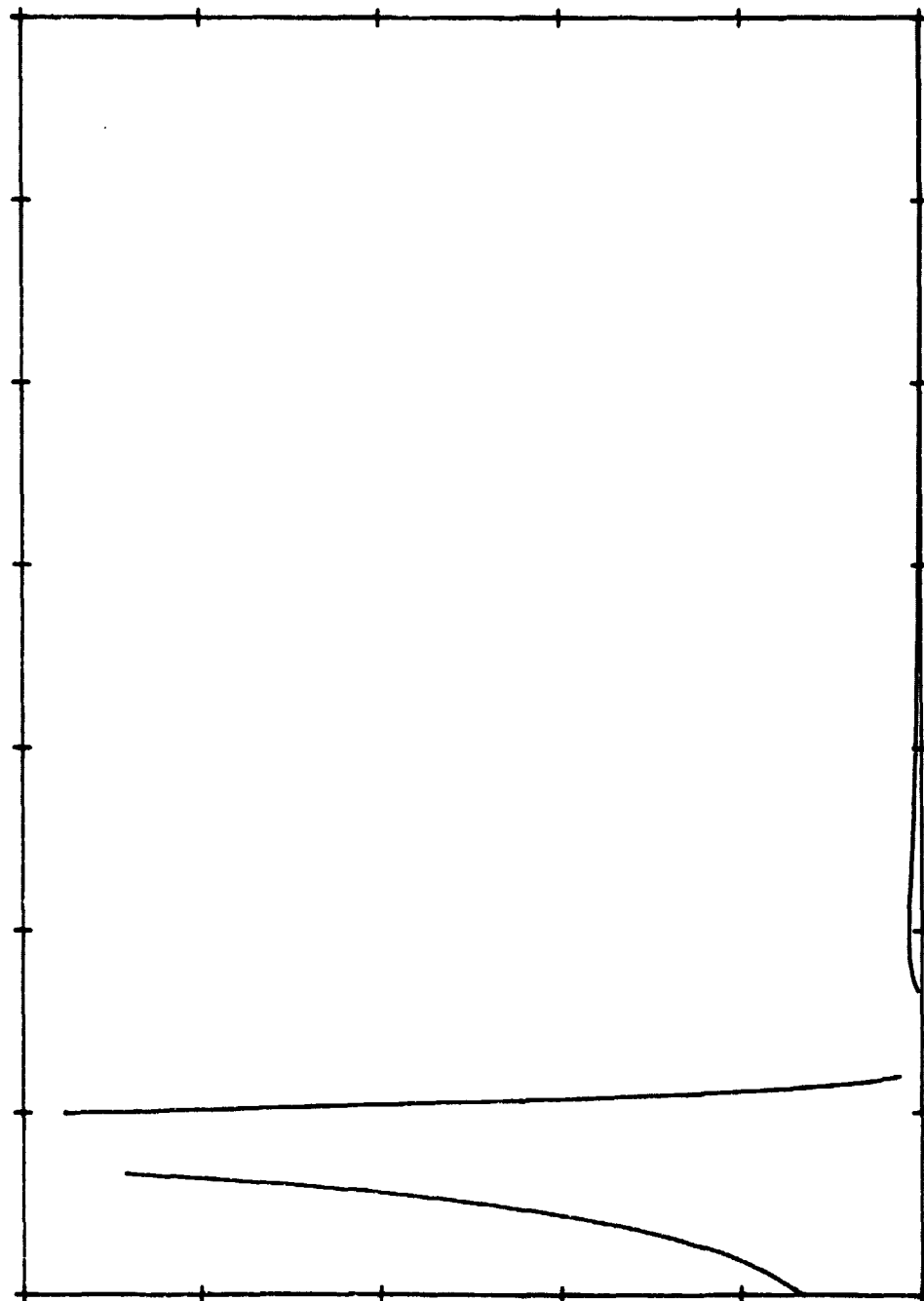
- 1) surface roughness
- 2) surface dielectric constant
- 3) pole orientation, and
- 4) rotation rate

Dick Simpson

VOYAGER

ECHO HALF POWER BANDWIDTH

5.000E 03



ORIGINAL PAGE 10
OF POOR QUALITY

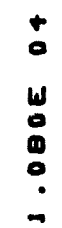
1.080E 04

TIME

-1.800E 03

0.000E-01

TITAN BSR .. VOYAGER
TODAY TO. BSR. 1. 7. 15-47-35



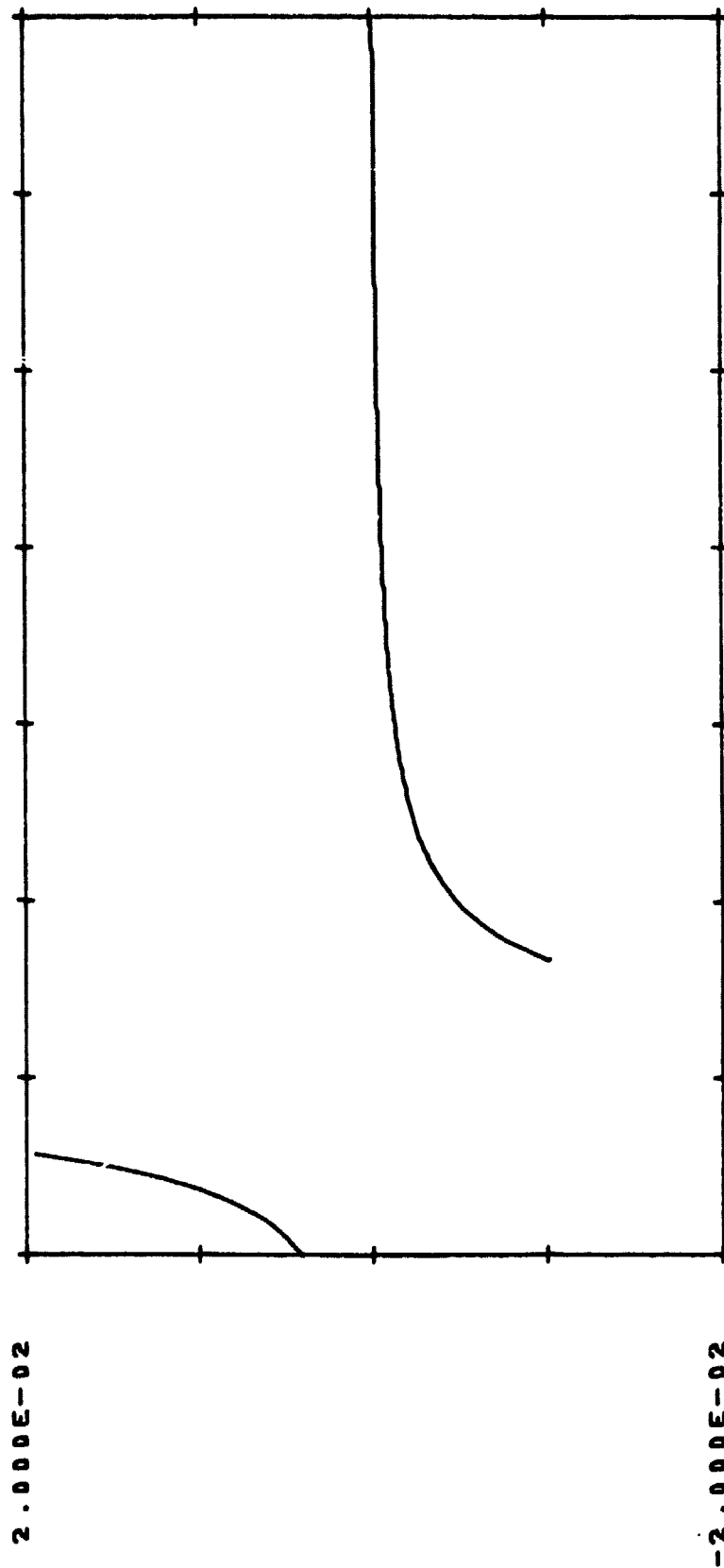
TIME

-1.800E 03

TI 2000E-02
VTUAVO X004 0

ORIGINAL PAGE IS
OF POOR QUALITY

TIME DERIVATIVE OF SPECULAR ANGLE (DEG/SEC)



1.080E 04

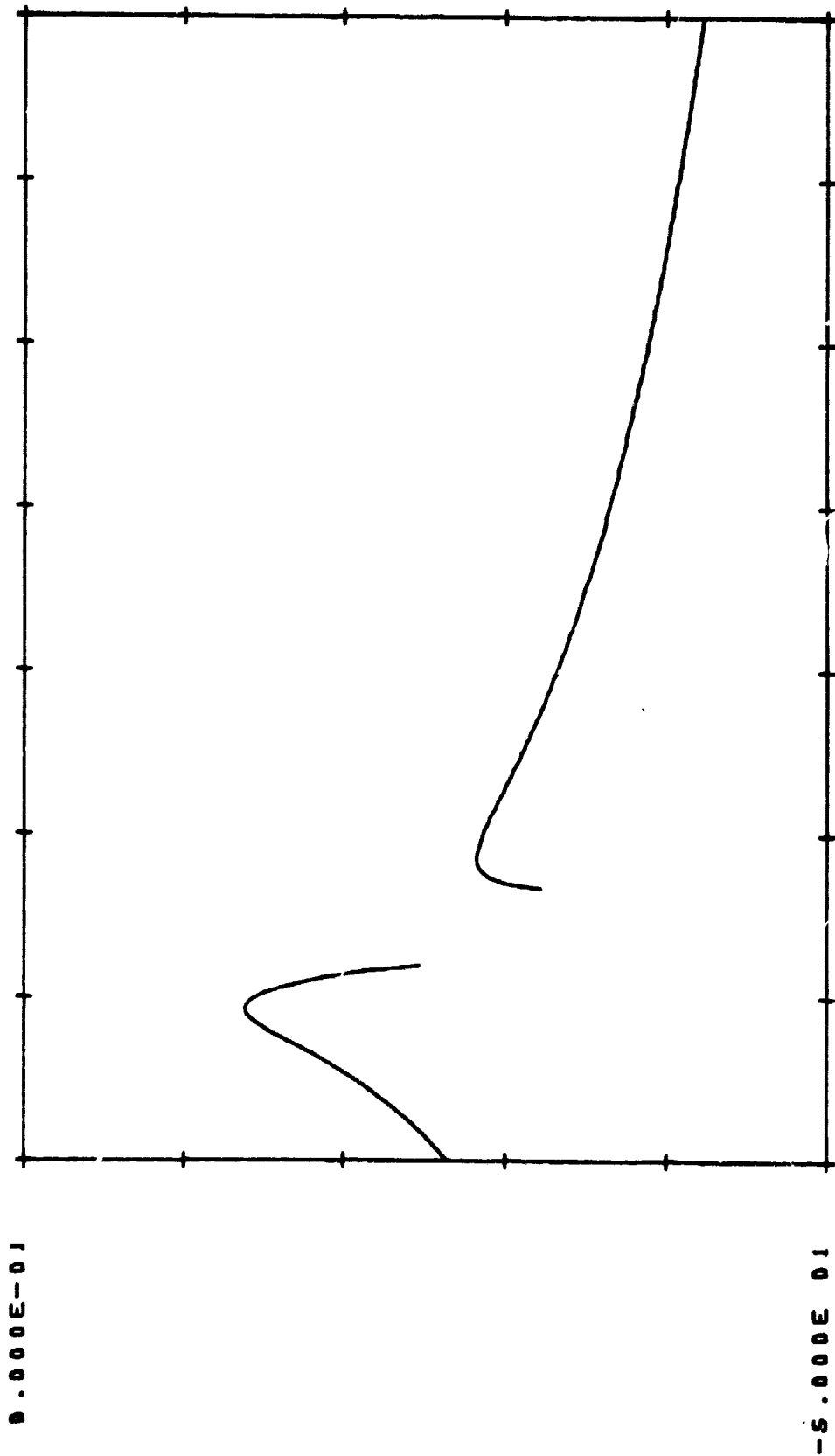
TIME

-1.800E 03

-2.000E-02

2.000E-02

STRENGTH OF INTEGRATED ECHO WRT DIRECT (DB)



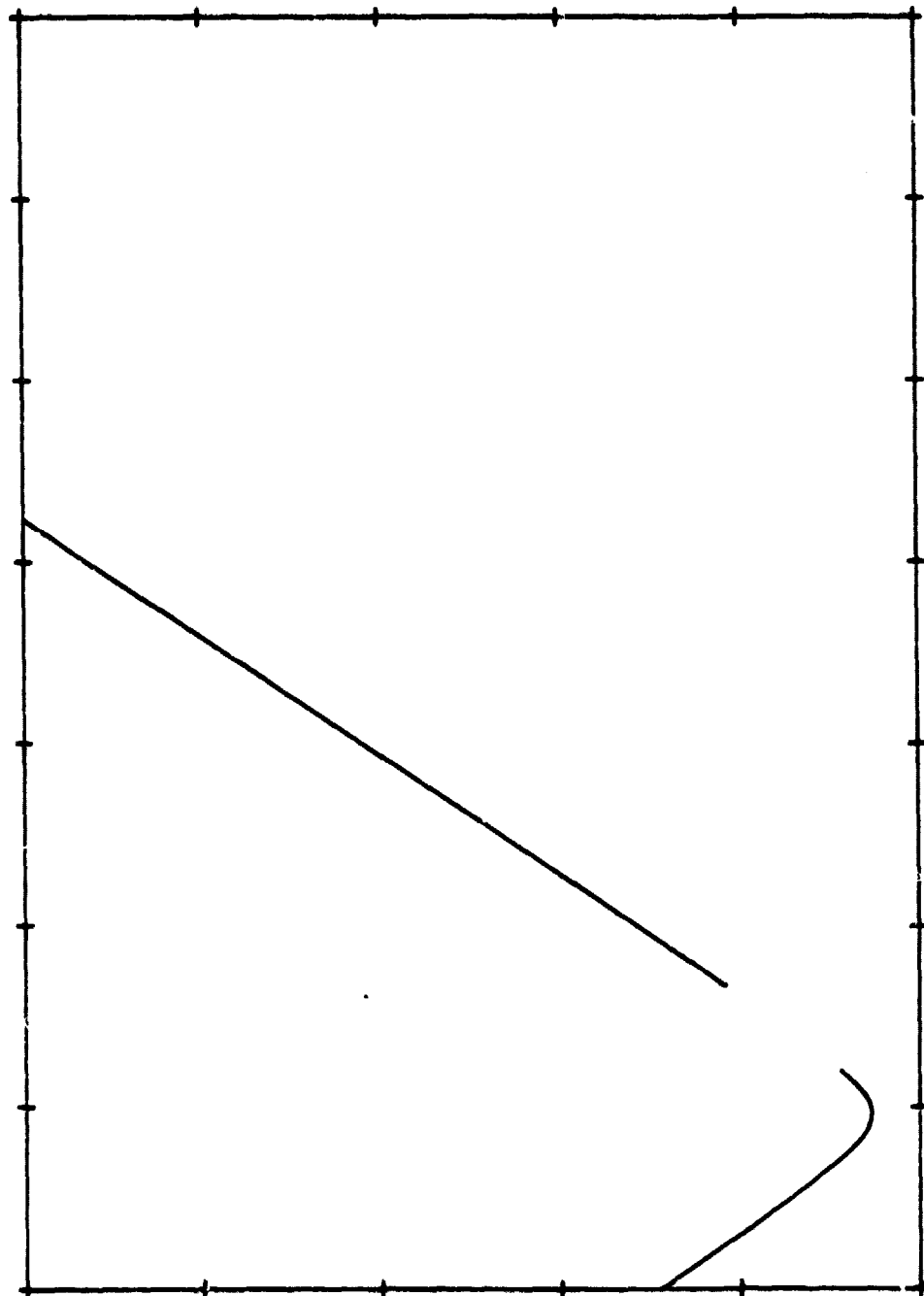
ORIGINAL PAGE 18
OF POOR QUALITY

TITAN BSR .. VOYAGER
FORM 15- 02- 1 1 7 18-18-44

SPACECRAFT TO SPECULAR POINT DISTANCE

1.000E 08

0.000E-01



ORIGINAL PAGE IS
OF POOR QUALITY.

1.080E 04

TIME

-1.800E 03

TITAN SRV ... VOYAGER

REFLECTED DOPPLER OFFSET

1.500E 05

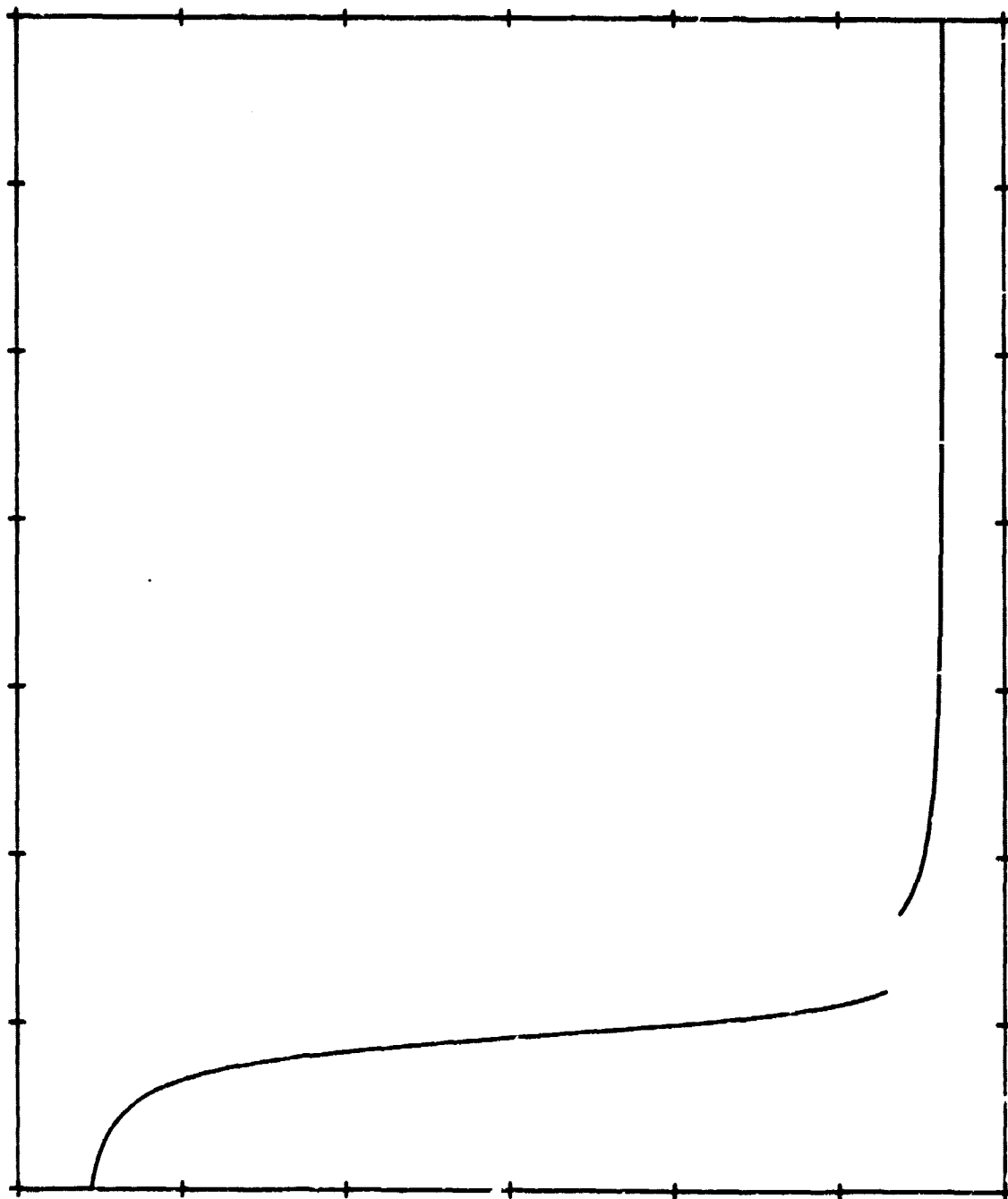
-1.500E 05

ORIGINAL PAGE IS
OF POOR QUALITY

1.000E 04

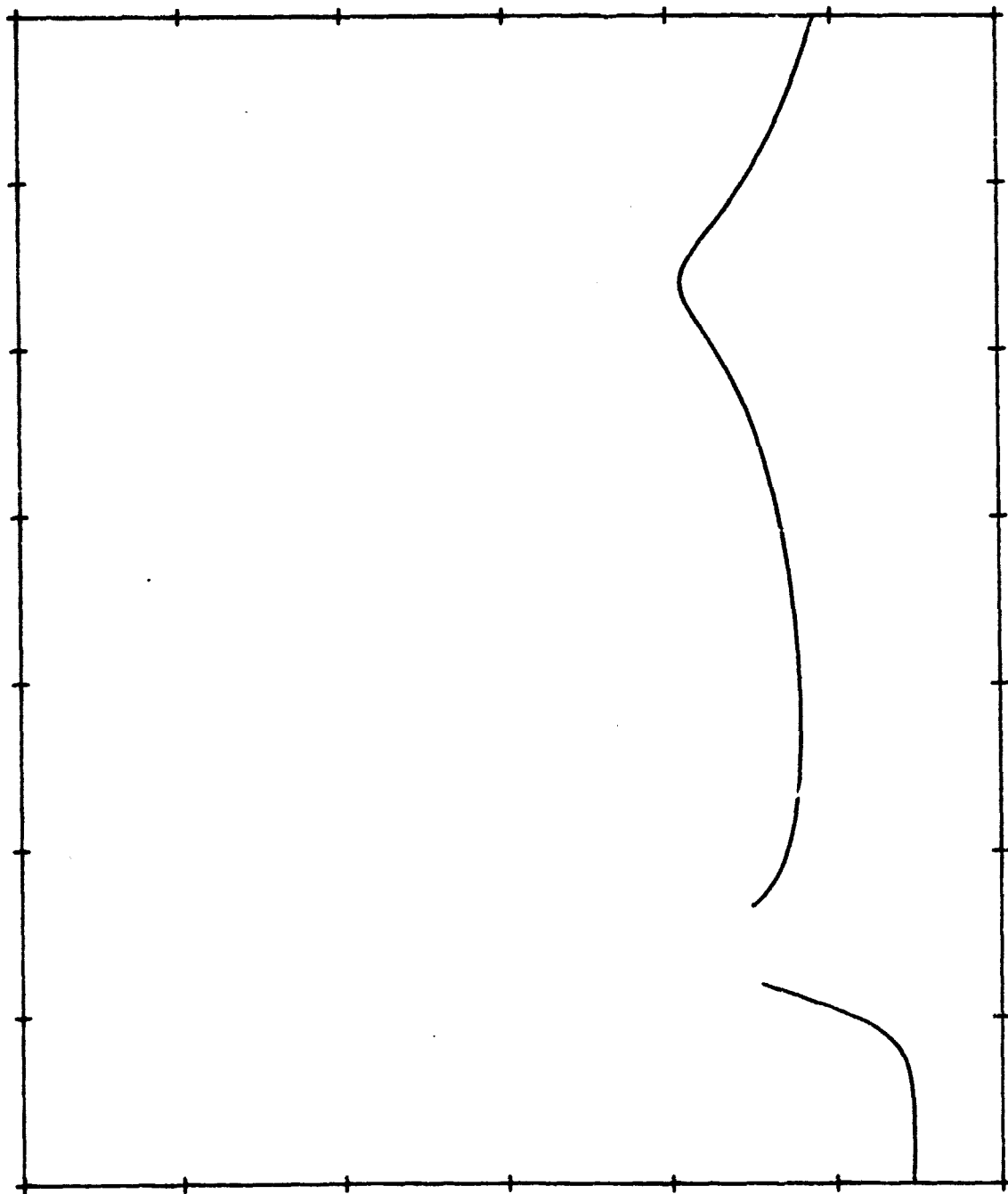
TIME

-1.000E 03



DETECTABILITY, LS DIV BY BW (DB)

0.000E-01



-6.000E 01

1.080E 04

TIME

-1.800E 03

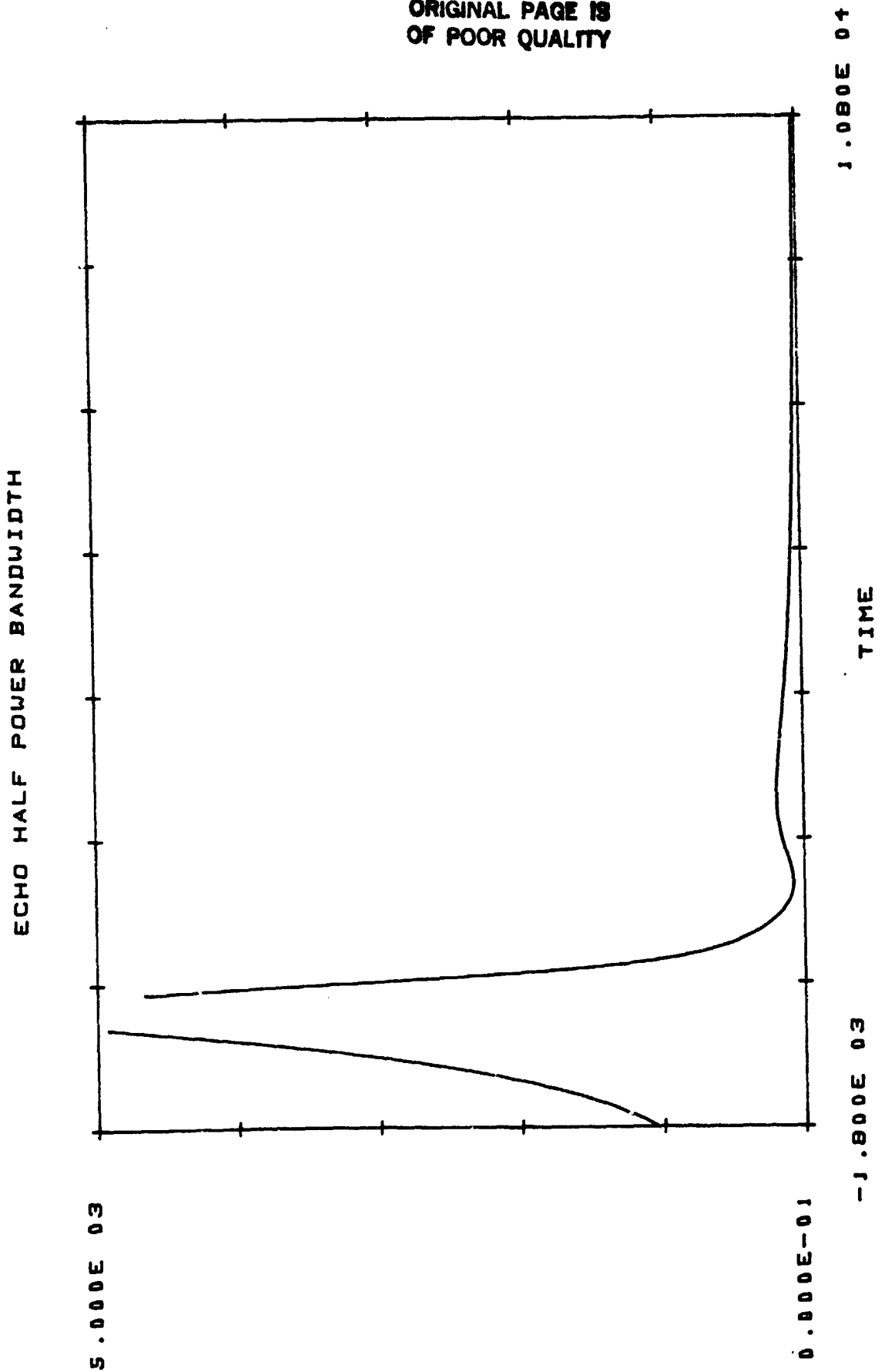
ORIGINAL PAGE IS
OF POOR QUALITY

TITAN BSR ... VOYAGER
TITAN BSR ... VOYAGER

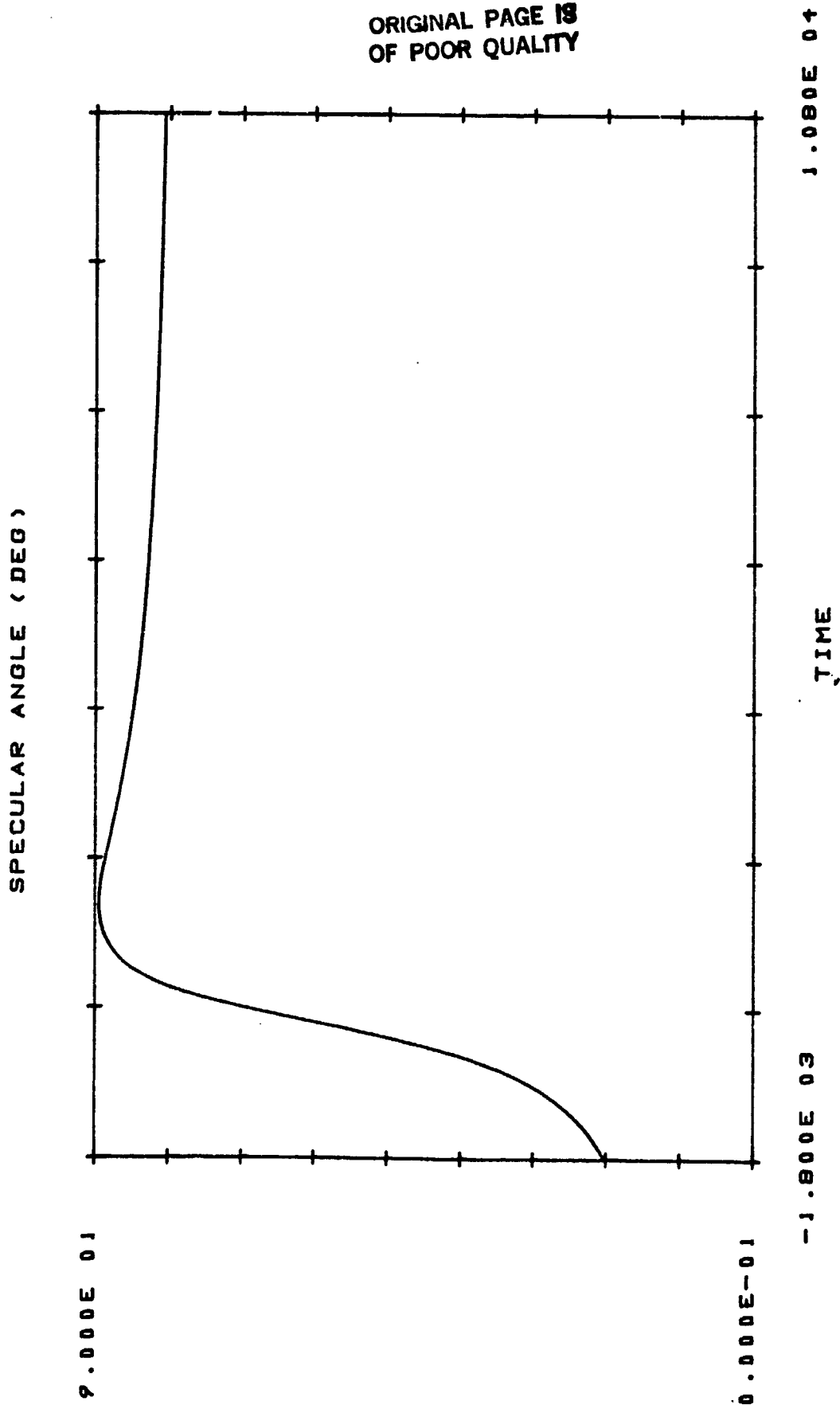
SATURN GALILEO
EQUATORIAL TOUR

TITAN, BEB ... SATURN DAILYED ... EQUATORIAL ORBIT
TODAY, IC. 02. 1. 2. 13. 13. 4

ORIGINAL PAGE IS
OF POOR QUALITY



ORIGINAL PAGE 18
OF POOR QUALITY



TIME DERIVATIVE OF SPECULAR ANGLE (DEG/SEC)

2.000E-02

-2.000E-02

ORIGINAL PAGE IS
OF POOR QUALITY

-1.800E 03

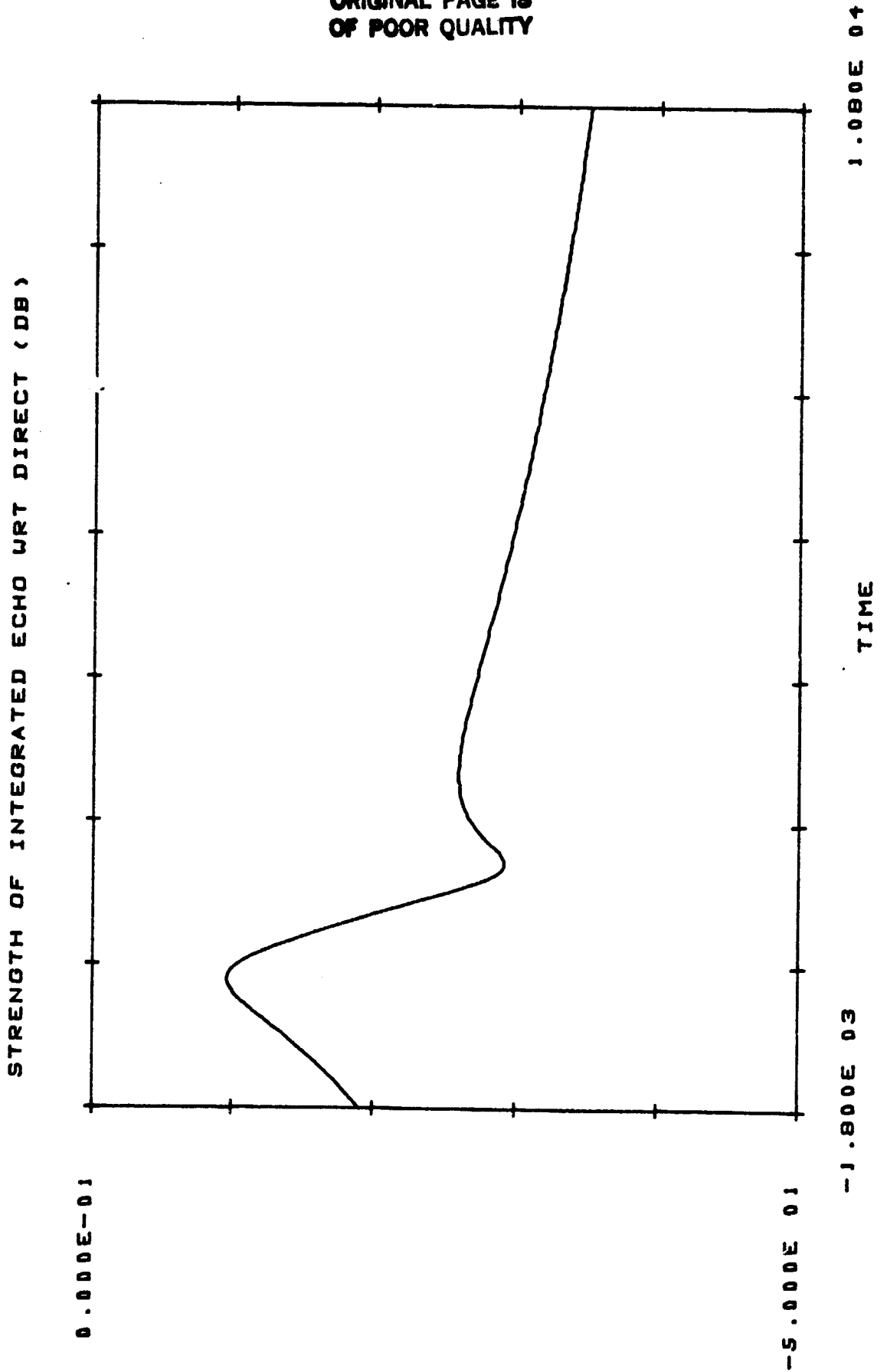
TIME

1.080E 04

TITAN, BEAR ... SATURN BALILO ... EQUATORIAL ORBIT
TITAN, BEAR ... SATURN BALILO ... EQUATORIAL ORBIT

TITAN SR ... SATURN VALERO ... EVALUATION DESIST

**ORIGINAL PAGE IS
OF POOR QUALITY**



SPACECRAFT TO SPECULAR POINT DISTANCE

1.000E 08

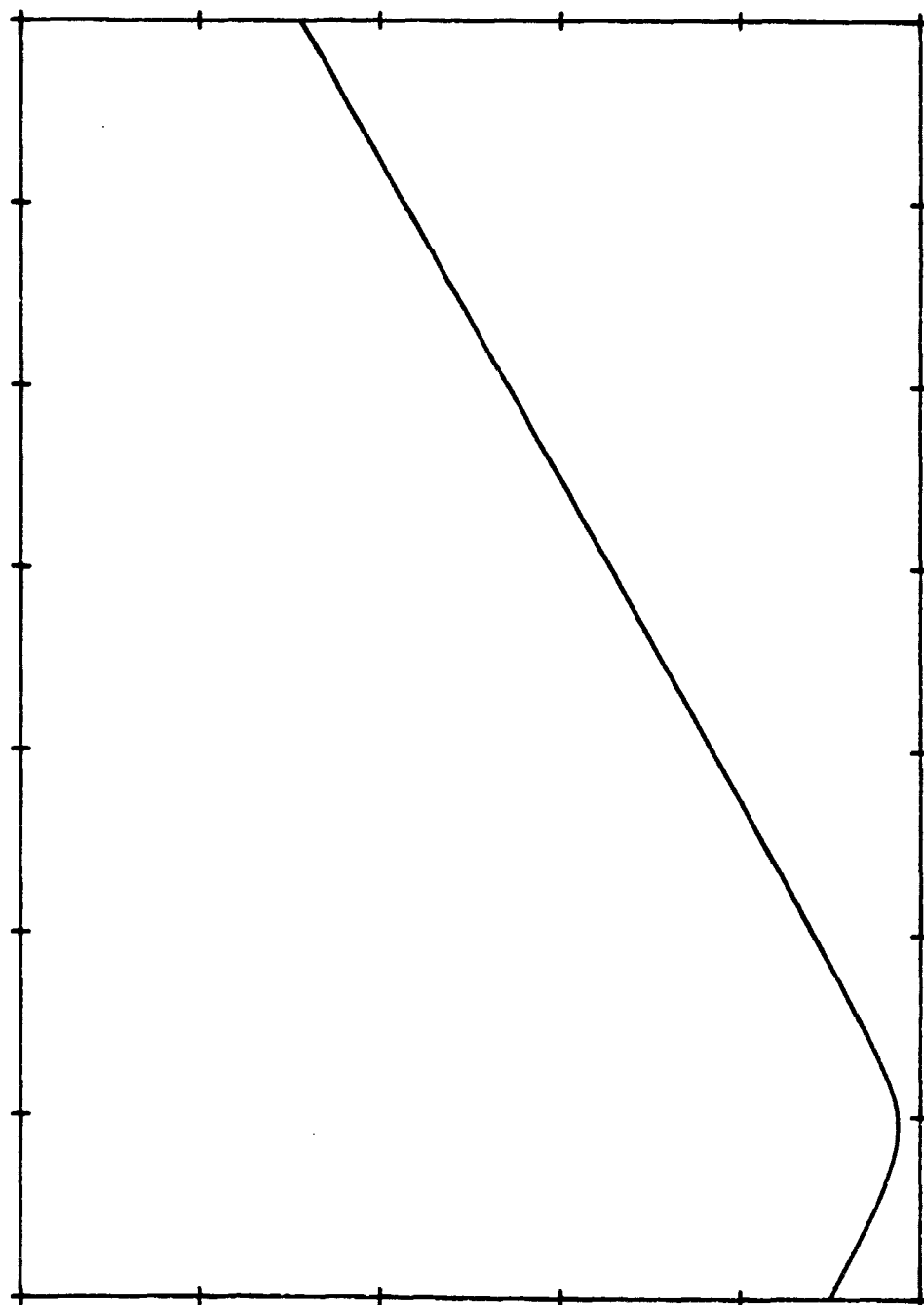
0.000E-01

ORIGINAL PAGE IS
OF POOR QUALITY

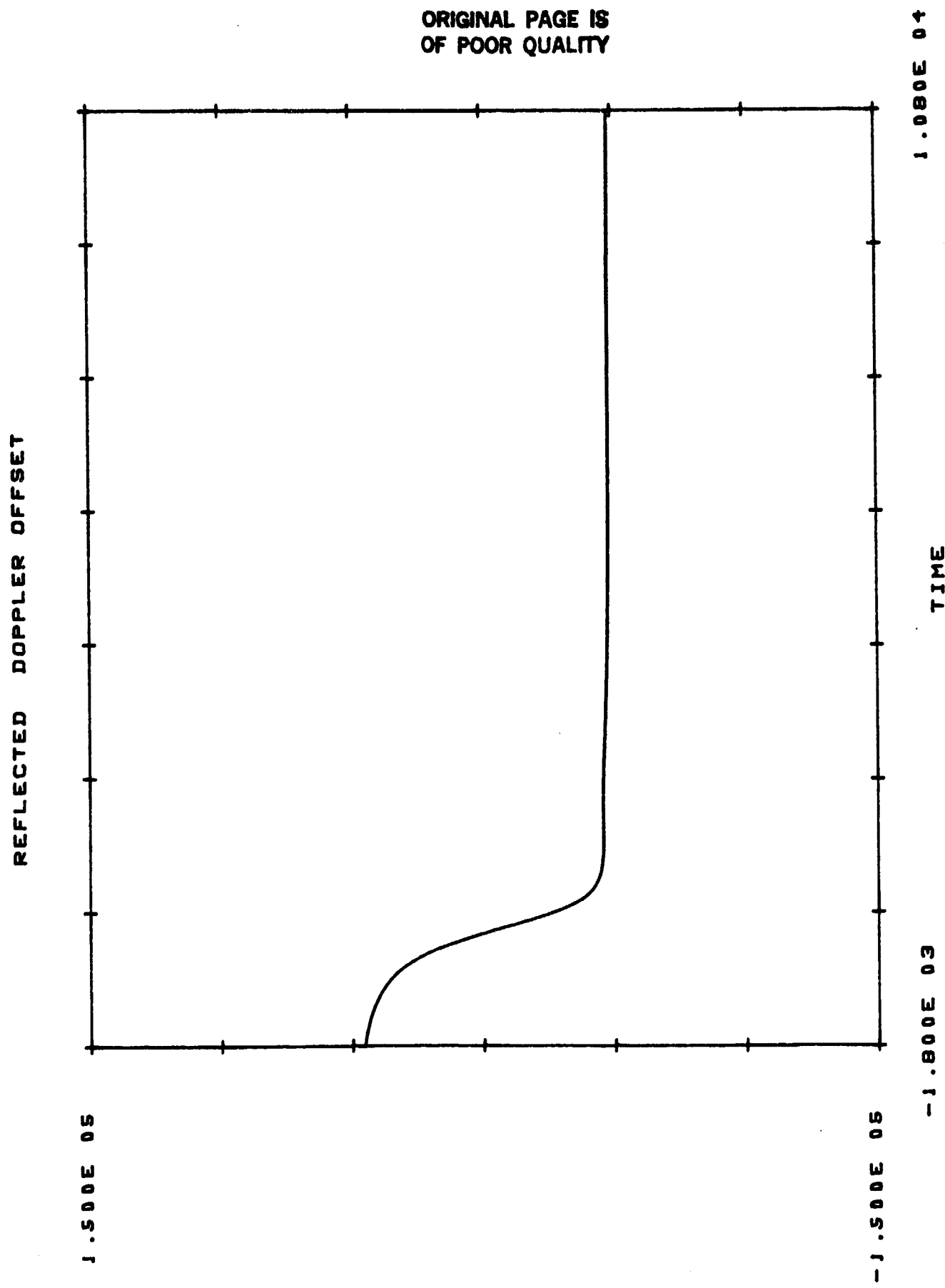
1.080E 04

TIME

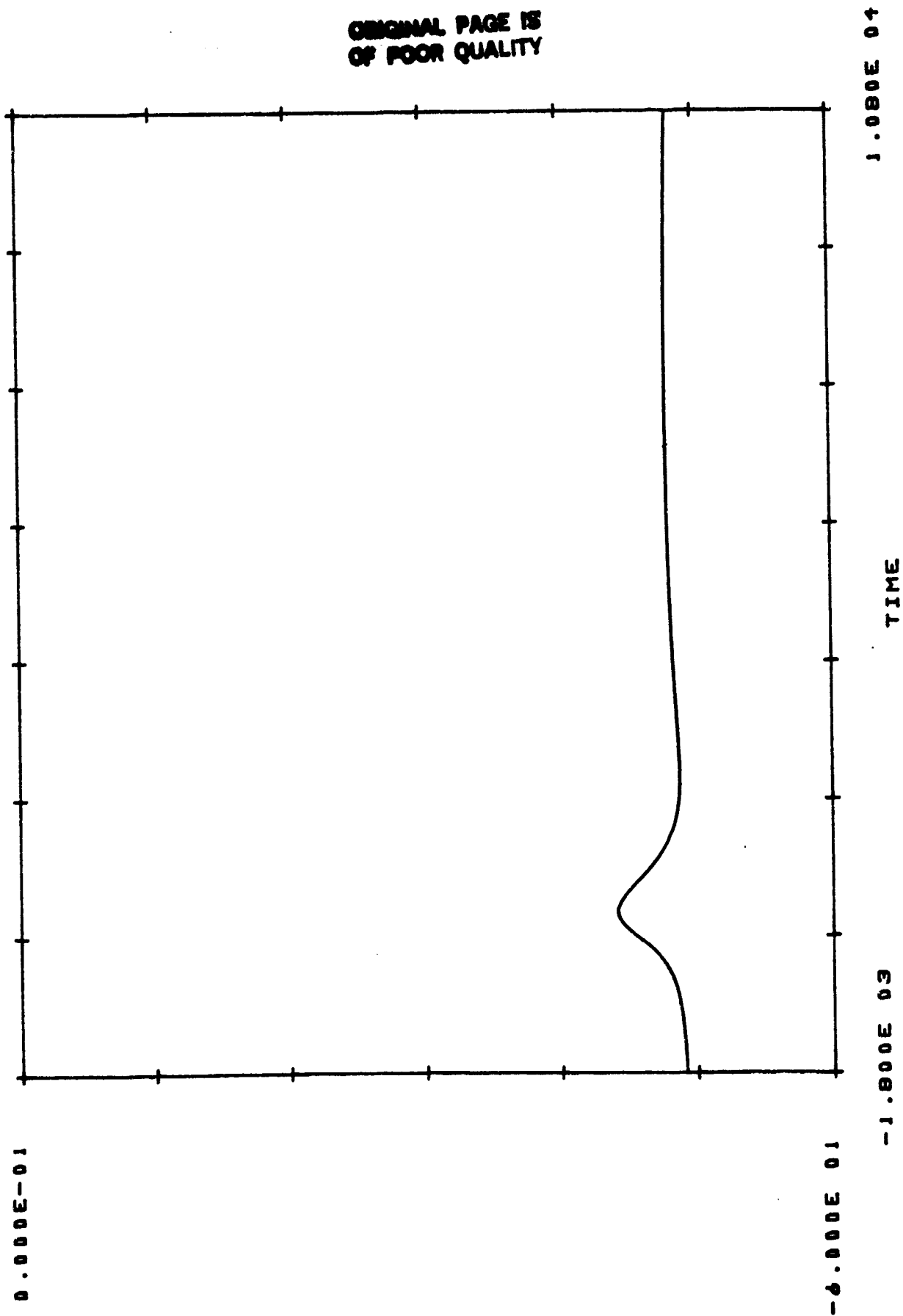
-1.800E 03



ORIGINAL PAGE IS
OF POOR QUALITY



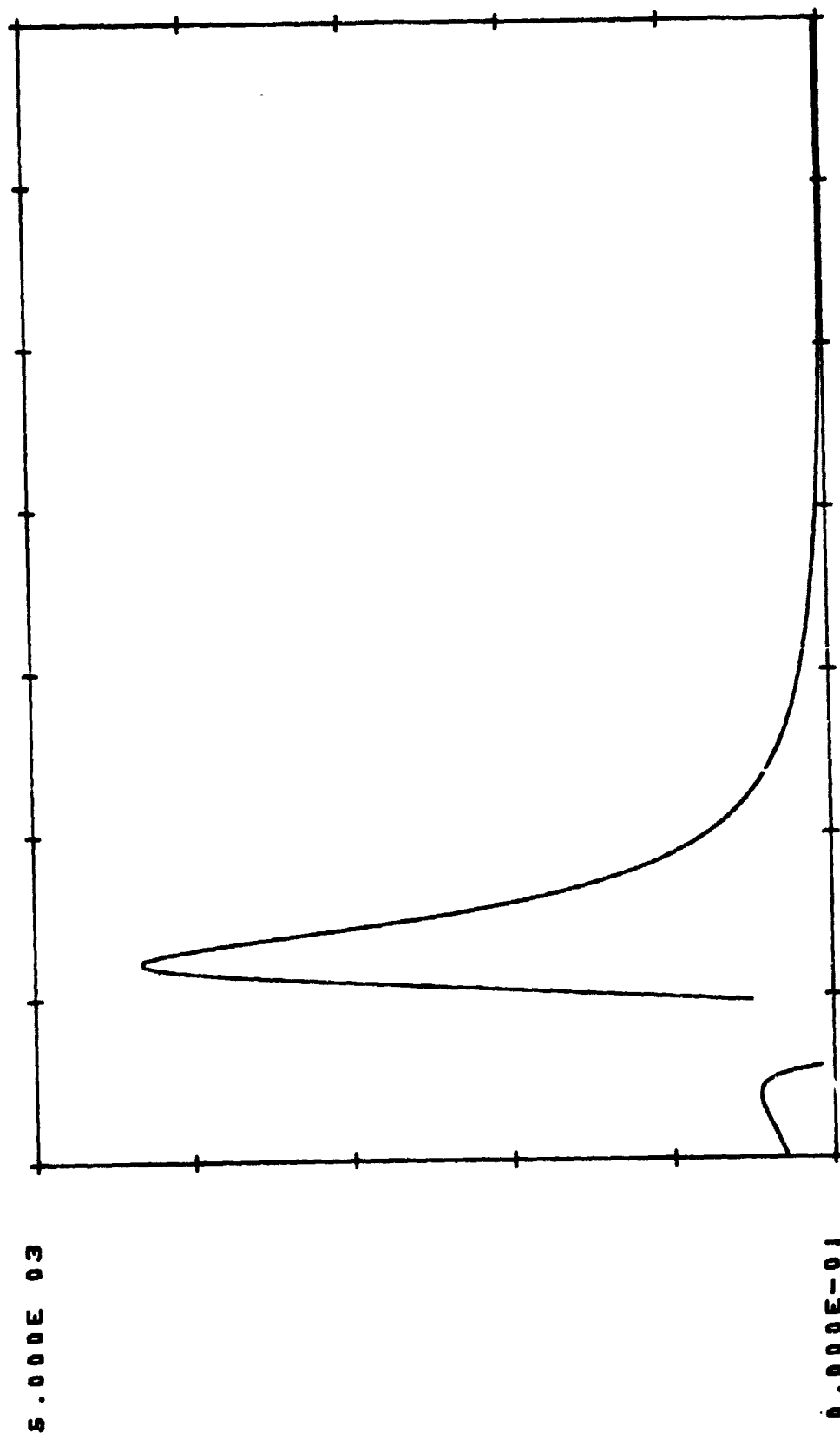
DETECTABILITY, LS DIV BY BW (DB)



SATURN GALILEO

POLAR TOUR

ECHO HALF POWER BANDWIDTH

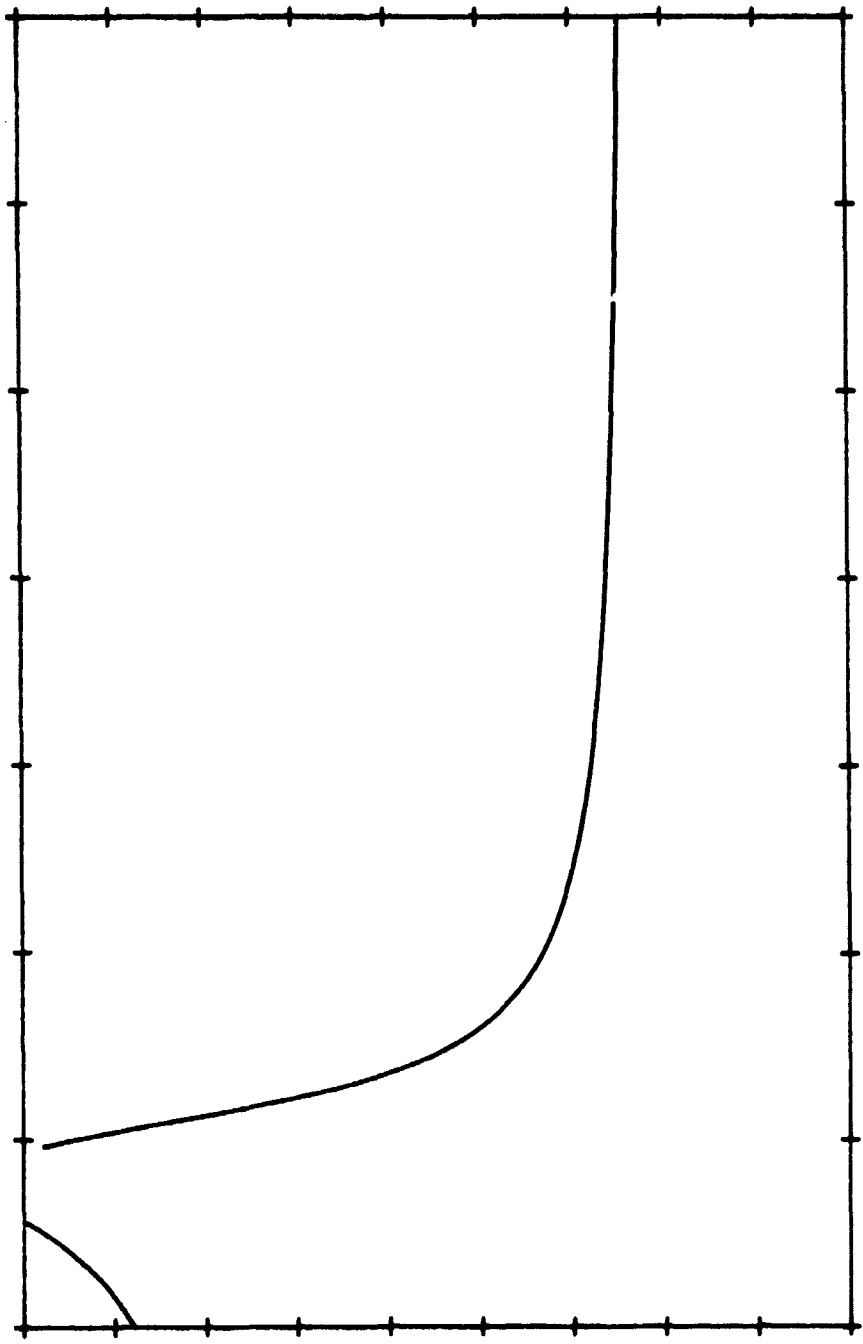


ORIGINAL PAGE 13
OF POOR QUALITY

TITAN SR ... RETURN CALLED ... POLAR ORBIT
TITAN SR ... RETURN CALLED ... POLAR ORBIT

ORIGINAL PAGE IS
OF POOR QUALITY

SPECULAR ANGLE (DEG)



1.000E 04

TIME

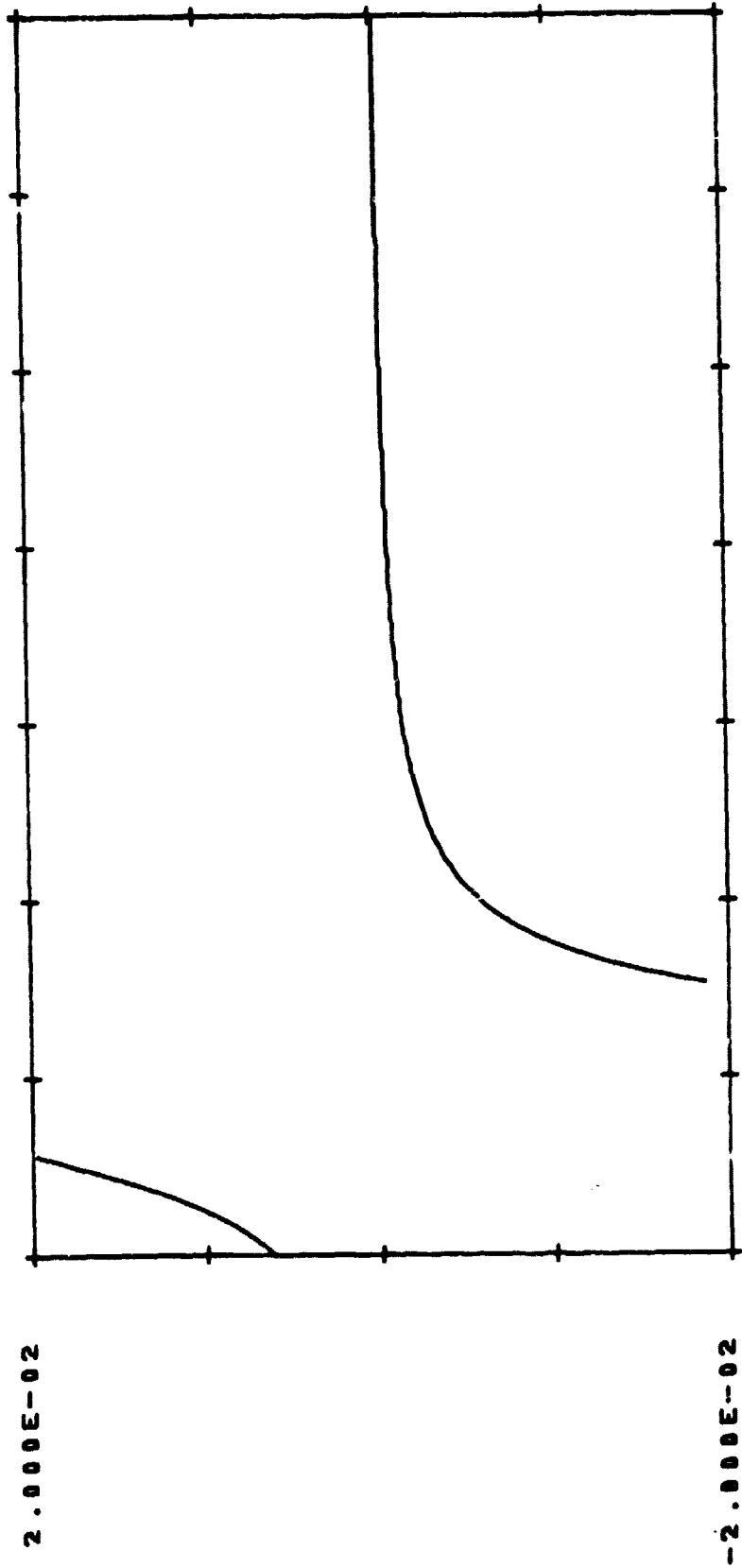
-1.800E 03

0.000E-01

9.000E 01

ORIGINAL PAGE IS
OF POOR QUALITY

TIME DERIVATIVE OF SPECULAR ANGLE (DEG/SEC)



1.080E 04

TIME

-1.800E 03

-2.000E-02

2.000E-02

717AN BEN .. SATURN VALLEY .. POLAR ORBIT
UNITS 10, 20, 30, 40

ORIGINAL PAGE IS
OF POOR QUALITY

S:LENGTH OF INTEGRATED ECHO WRT DIRECT (DB)

10-300-01

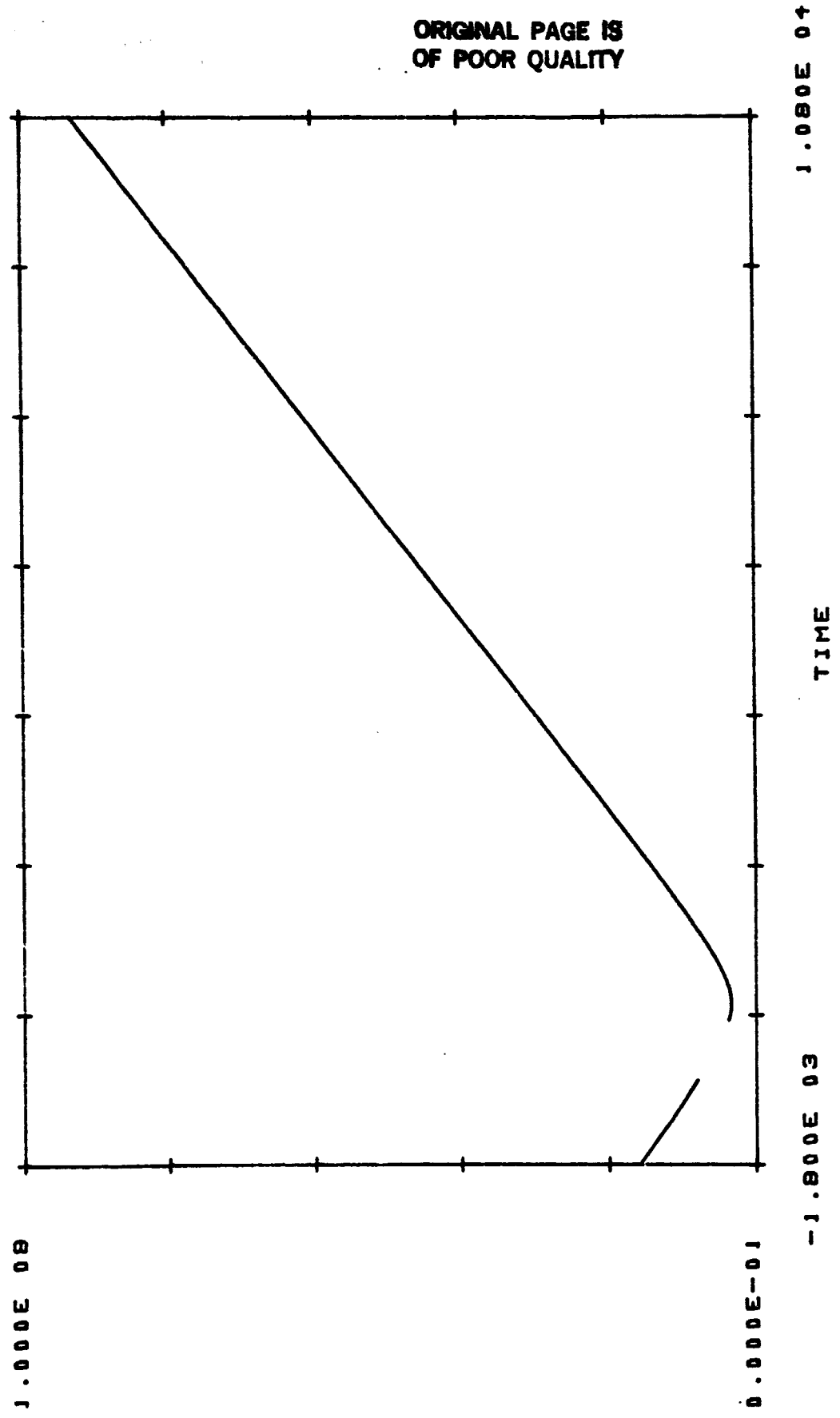
10-3060-5-

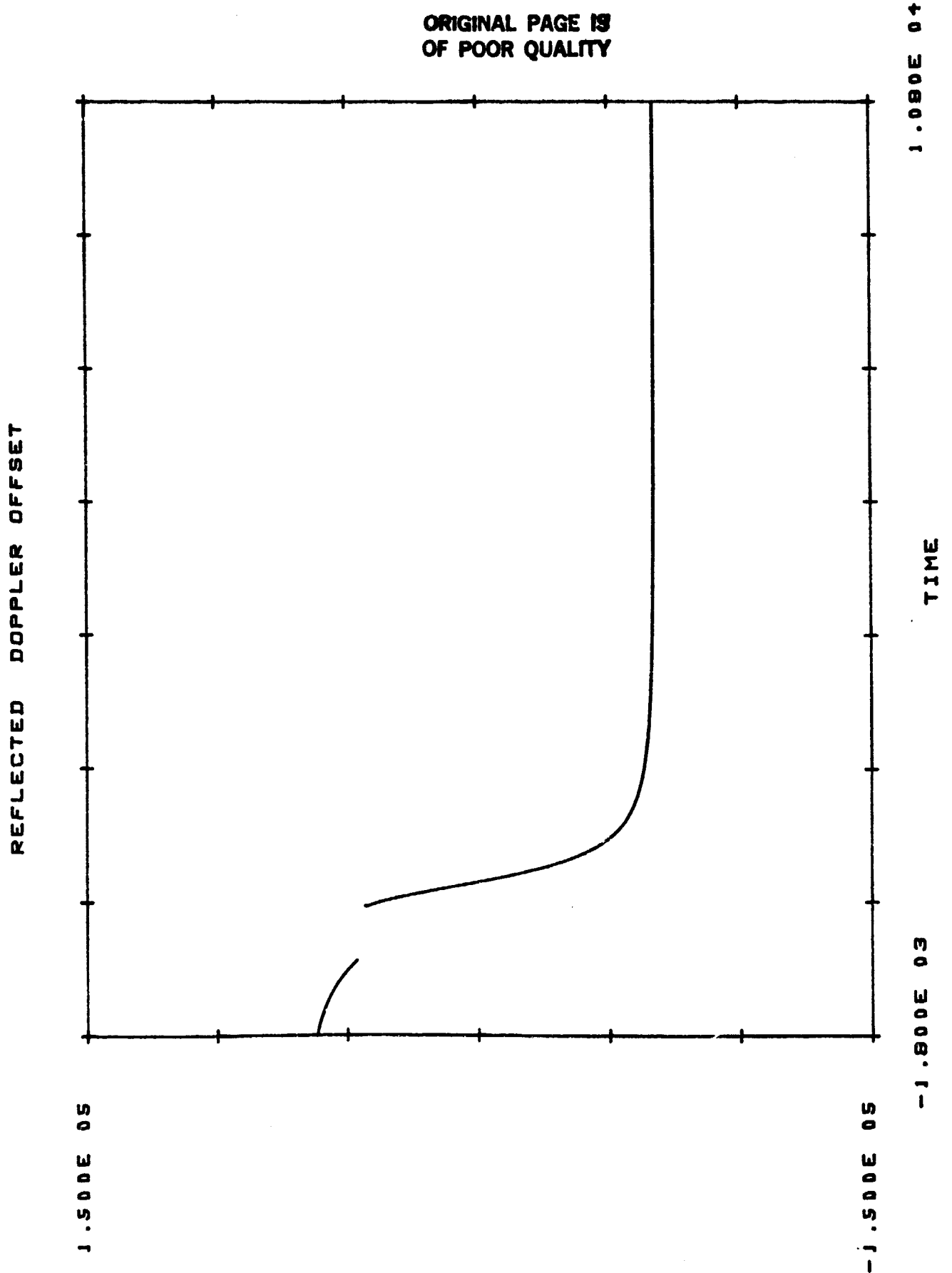
-1.800E 03-

TIME

1.080E 04

SPACECRAFT TO SPECULAR POINT DISTANCE





DETECTABILITY, LS DIV BY BW (DB)

0.000E-01

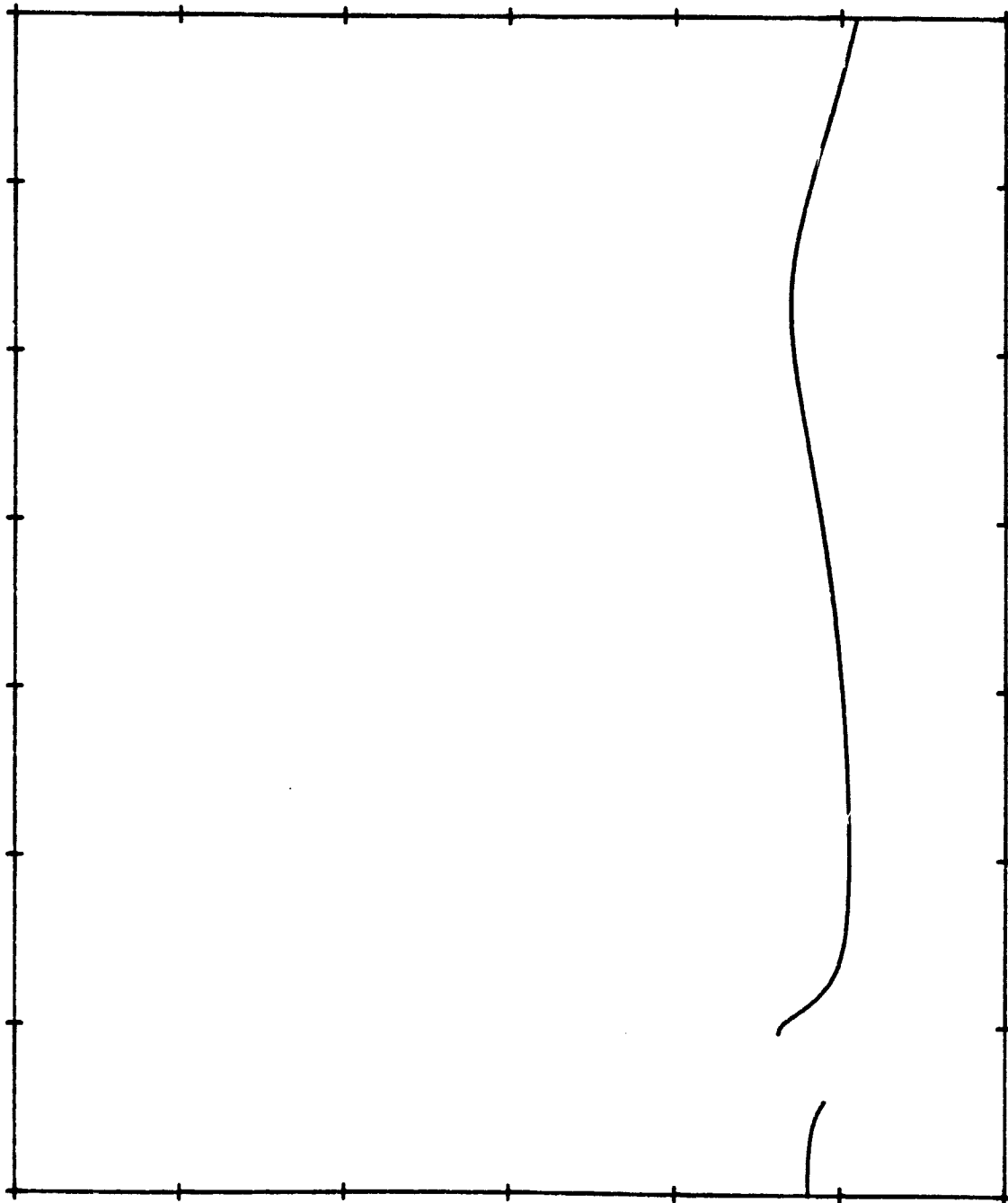
-4.000E 01

-1.800E 03

TIME

1.080E 04

ORIGINAL PAGE IS
OF POOR QUALITY



TITAN SER ... SATURN CALLED ... POLAR ORBIT
TOTAL TO ... 1.2 15.71.77

PROGRESS IN DATA ANALYSIS:
NEW TECHNIQUES FOR INTERPRETING RADIO SCINTILLATIONS
DURING PLANETARY OCCULTATIONS

D. P. Hinson, G. L. Tyler, and V. R. Eshleman

The exploration of the Jovian and Saturnian systems using Voyagers 1 and 2 included 3.6 cm and 13 cm wavelength radio observations during occultations of the spacecraft by Jupiter, Saturn, and Titan. One of several areas of research based on these observations involves the way that refractive irregularities in the atmospheres of these planets caused amplitude and phase scintillations at both wavelengths. In conjunction with the reduction and analysis of these data (which was funded under a separate grant), we have developed new techniques for interpreting the scintillations observed during planetary occultations; each is described briefly below. In particular, there has been a significant improvement in the procedure used to analyze scintillation spectra. Moreover, application of this methodology to the Titan occultation data has yielded unique results which should help to resolve a long-standing controversy as to the nature of the atmospheric irregularities which cause scintillations during planetary occultations.

Analysis of Scintillation Spectra. In this new procedure, measured temporal spectra of the weak fluctuations in amplitude and phase are interpreted using conventional methods of spectral data analysis and the well-developed theory for weak scattering. The occulting atmosphere is modeled as a thin screen containing a power-law distribution of anisotropic irregularities. Comparisons of measured scintillation spectra with the theory produce least-squares solutions for four parameters which characterize the

underlying atmospheric scattering structures. The parameters are: (1) the axial ratio, (2) the orientation, (3) the power-law exponent of the spatial spectrum, and (4) the magnitude of the spatial variations in refractivity. In order to determine the measurement uncertainties, the covariance matrix of the solutions for the four parameters is calculated by standard propagation of errors.

Previous methods for analyzing the scintillation spectra relied on a simple visual comparison between the theory and the measurements, and provided no uncertainties in the results. The improvement offered by the new procedure is best illustrated through an example. We have analyzed the radio scintillations observed during the occultations of the Voyager spacecraft by the ionospheres of Jupiter (Hinson and Tyler, 1982, JGR, 87, 5275-5289) and Saturn (Hinson, 1983, JGR, in press). In particular, the magnetic field orientation at locations near these planets has been inferred from the occultation data, along with the associated uncertainties. These measurements are of interest because they provide a test of current Jovian and Saturnian magnetic field models, which were derived from spacecraft magnetometer measurements. In this regard, the uncertainties in the occultation measurements are of fundamental importance in evaluating the field models -- without uncertainties, the results derived from previous occultation studies are difficult to interpret. Hence, this new procedure has extended the capability of the radio occultation method.

The Signature of Atmospheric Internal Gravity Waves in Occultation Measurements. In a wind-free isothermal atmosphere, the amplitude of internal gravity waves propagating without attenuation increases exponentially with altitude. Real planetary atmospheres have nonuniform temperature profiles; this thermal structure imposes additional variations in wave amplitude with

height. The vertical wave envelopes can be calculated for each of the planetary atmospheres studies during spacecraft flybys on the basis of radio occultation measurements of temperature-pressure profiles and a linearized theory for atmospheric waves.

The density disturbances associated with atmospheric waves perturb the occultation radio signals. Under conditions of weak scattering, the fractional variance of received signal intensity is proportional to the variance in density. Hence, the presence of internal gravity waves can be established through a comparison of the theoretical calculations described above with the measured profile of the residual intensity variance (after the removal of average effects). In this manner, the signature of freely propagating internal gravity waves in Titan's upper atmosphere has been identified in the Voyager 1 radio occultation data (Hinson and Tyler, 1983, Icarus, 54, 337-352). Above 25 km, the altitude dependence of the measured intensity variance appears to be explained entirely by modulation of internal gravity waves by the atmosphere's average vertical structure.

Signal scintillations are a common feature of the observations during both radio and stellar occultations; this new method of analysis should lead to a better understanding of atmospheric effects in occultation measurements. In principle, this same procedure can be applied to the study of Venus, Mars, Jupiter, Saturn, Uranus, and Neptune.

Clouds in planetary atmospheres

We have considered idealized experimental approaches for using the radio occultation technique to study cloud systems in planetary atmospheres. A summary account is given here of our general conclusions concerning experiment design and types of measurements. As one result of this investigation, we have prepared and submitted to NASA a proposal to use the Pioneer-Venus orbiter for studies of the cloud region in the middle atmosphere of Venus (Stanford proposal number RL 38-83, submitted August, 1984, for Radio Science Experiments during the Pioneer Venus Extended Mission). That is, while Pioneer Venus does not provide the idealized radio science "instrument" in the sense given above, it appears that it has significant potentialities of a type that have not yet been realized for this purpose.

The general requirements for optimum radio propagation studies of the cloud regions in planetary atmospheres include:

1. Highest feasible SNR (signal-to-noise-ratio).
2. Best possible frequency stability.
3. Best possible amplitude stability.
4. At least two and preferably more radio wavelengths, including one sub-centimetric wavelength.
5. Orthogonal signal polarization measurements including a pair at a sub-centimetric wavelength.
6. Spacecraft orientation control for limb tracking and bistatic sounding of the surface.
7. Dual spacecraft.

Number (1) involves spacecraft and ground based transmitter powers, antenna sizes, receiver noise figures and bandwidths, and operating radio

frequencies. There is a long history of continuing efforts for improvements in these areas by the Deep Space Net, in its efforts to advance the state of the communications art for the radio links between distant spacecraft and the Earth. Essentially all improvements in these areas directly benefit radio science experiments. Item (2) has also been of prime concern to the DSN, but with emphasis only on the ground terminal. A new level of stability on the spacecraft was achieved with the USO (the so-called ultra stable oscillator) introduced for radio science on the Voyager missions. The USO constitutes an extraordinary example of the value of a modification to the communications and tracking systems for the purpose of improving radio science. Fundamentally important aspects of the atmospheric and ring occultation experiments, and certain tests of the theory of relativity, were possible with Voyager only because of the USO. Still greater spacecraft oscillator stability is possible for future missions, and would directly benefit measurements of atmospheric structure at precisions that would be important in helping to determine the effects of condensibles.

Amplitude stability (item 3) has not been an area that has been emphasized (except for the usual high standards of engineering followed by the DSN), since there are no stringent requirements for the communications and tracking applications. For the study of cloud regions and their associated absorbing vapors, however, amplitude stability factors directly into the accuracy of the absorptivity measurements. Thus this is a key requirement for cloud studies. The ability to measure small amplitude changes with accuracy involves not only the knowledge of transmitter powers and receiver gains, but also antenna gains in the propagation directions for both the spacecraft and ground-based antennas. This implies stringent requirements on the knowledge of the pointing of these high gain antennas. There is much to be gained in

the potential of future cloud studies from a concerted effort to improve our knowledge and control of signal amplitudes.

The history of the debate over the need for multiple radio frequencies or wavelengths in spacecraft radio experiments (item 4) goes back to the time of the first deep-space missions. The joint advantages of the S and X band systems for communications, tracking, and science resulted in their eventual development, and has thus far led to their continued use. For cloud studies, multiple wavelengths are important on at least four counts. First, they allow self-calibration of plasma effects on the long links to Earth, for greater profile accuracies. Second, the dependence of absorptivity on wavelength can help identify and characterize the cloud vapors and possibly the particulate absorbers. Third, signal scintillations (amplitude and phase) at several wavelengths give a more complete picture of small-scale atmospheric structures that may be related to the effects of the latent heat on the cloud condensibles, convective instabilities, and internal gravity waves. And fourth, the use of a relatively short wavelength may make it possible to measure the depolarizing properties of large cloud particulates, as discussed next.

Depolarization has been measured on radio propagation paths between communications satellites and ground tracking stations. Moreover, the character of the depolarization has been observed, on occasion, to change suddenly. It is believed that the depolarization is due to ice crystals and that the changes accompany disorientation or reorientation of crystals that initially were aligned by atmospheric electric fields. That is, the sudden changes have been observed to accompany lightning discharges. Thus it is possible that polarization measurements on occultation paths through the atmospheres of the planets (item 5) would provide information on the number

and size of certain cloud particulates, about their shapes and orientations, and about sudden changes in electric fields in these atmospheres. The emphasis on relatively short wavelengths for such measurements is because such effects would then be accentuated.

Spacecraft orientation control (item 6) is related to the pointing accuracy problem as described for item 3 on amplitude stability. In addition, it may be possible to obtain limited data on cloud related properties for regions below the level of critical refraction by a bistatic radar bounce off the surface. This is particularly relevant to Venus, where the occultation measurements can probe down only to about 33 km altitude. Much of the region of interest for Venus cloud studies lies above this height, but absorption by cloud related gases certainly occurs in the lower regions that can only be reached by such a radar bounce. For this experimental approach, it would be necessary to study also the scattering properties of the surface, since they must be known to determine the atmospheric absorption along the carom path.

Two or more spacecraft simultaneously in orbit around the target planet (item 7) would provide, in principle, two methods for improving the accuracy of occultation experiments. Consider one spacecraft in atmospheric occultation and the other well away from the planet in the plane of the sky. Simultaneous radio links from both to the Earth would provide atmospheric occultation signals, plus "calibrating" signals that traverse essentially the same path in interplanetary space and in Earth's atmosphere and ionosphere. Thus the effects of the planetary atmosphere could be isolated more thoroughly than in the one-spacecraft method. The other possibility for multiple spacecraft is for the occultation radio link to be between pairs of orbiting spacecraft. The signal characteristics could then be measured with the information sent to Earth by telemetry. Because these occultation paths would

be very short compared to the distance to Earth, higher SNR and less contamination by terrestrial and interplanetary media could be obtained, in principle.

It would of course require considerable time, money, and effort to address all of the areas where significant improvements could be made in radio occultation studies of planetary atmospheres, with the above emphasis on the regions of clouds. It took many years to progress from single to dual frequency communications and tracking systems, and the USO is the only major example where a modification of these systems was made primarily for radio science. Thus it seems important to identify an order of priority. Assuming the continuance of dual frequency systems (4), we believe that the next order of priority is increased attention to improving the accuracy and reliability of amplitude measurements (3 and 6), and further improvement in frequency stability (2) for the spacecraft source beyond that presently provided by the USO or equivalent. The introduction of at least a third radio wavelength (shorter for some purposes and longer for others) would be next on our suggested agenda (4), with other proposed improvements being implemented when feasible.

**FINE-RESOLUTION RECONSTRUCTION OF THE MICROWAVE OPACITY
OF SATURN'S RINGS: THEORY, EXAMPLES, AND LIMITATIONS**

Essam A. Marouf

G. Leonard Tyler

Abstract

INTRODUCTION

Diffraction of radio waves is a prominent phenomena in measurements obtained during Voyager 1 radio occultation by Saturn's rings (Marouf and Tyler, 1984). It is caused by variations in the microwave opacity of the rings (optical depth at radio wavelength) on a radial scale comparable to or smaller than a characteristic dimension whose value is determined by the occultation geometry and observation wavelength (Fresnel zone radius F). For Voyager 1 geometry, $9 \lesssim F \lesssim 15$ km at 3.6 wavelength (λ) and is nearly twice as large at 13 cm- λ , setting a resolution limit of few tens of kilometers on opacity profiles obtained without corrections for diffraction. Although such resolution is certainly adequate for revealing a great deal of structure within the rings (Tyler et al., 1983), a much finer resolution becomes essential if the opacity profiles of the highly localized ring features discovered by Voyager (e.g., sharp edges, narrow ringlets and gaps, wave phenomenon) are to be properly mapped. A major objective of this paper is to develop inversion algorithms that correct for diffraction effects, hence improve achievable resolutions to values $\ll F$. For Voyager 1 at Saturn, the refined resolution is smaller than F by a factor ≈ 10 to 100, depending on the opacity of the region probed and the measurement errors. If Voyager 2 completes its planned occultation by Uranus' narrow rings successfully (January, 1986), a Fresnel zone radius ≈ 2 km at 3.6 cm- λ will make the need for diffraction corrections almost indispensable.

In radio occultation of planetary rings, opacity information is obtained from measurements of the average effects of ring material on an incident monochromatic plane radio wave traveling along the line-of-sight between a

spacecraft and the Earth. By utilizing an ultrastable oscillator to generate this wave, (Eshleman et al., 1977), not only the extinction of the direct wave emerging from the rings can be measured, but also its phase relative to that of the incident wave (hence the terminology "coherent signal"; Marouf et al., 1982). It is the ability to simultaneously measure the amplitude and phase of the coherent signal that makes the fine resolution reconstruction of the opacity profile possible. Such measurement correspond, in fact, to a one-dimensional sampling of the microwave hologram formed behind the rings. Starting from Fresnel-Huygens formulation of the diffraction problem and using a planar axially symmetric screen model for the rings, a Fresnel transform relationship between the complex amplitude measured (the hologram) and the microwave transmittance of the ring-model is shown to exist. The corresponding inverse transform provides the desired transmittance (hence, opacity) with resolution $\ll F$. Factors analyzed that affect post-inversion resolution are: uncertainties in F , finite curvature of ring contours, reference oscillator stability, and random measurement noise. Although the methods developed are general enough to be applicable at Uranus and also to be useful in guiding choices of optimum occultation geometries of future missions, our emphasis throughout this paper is on their application to the Voyager 1 occultation by Saturn's rings, where the geometry and selected examples of the measurements are used to illustrate the inversion theory and its limitations. Other examples are given by Tyler et al. (1983). A more complete diffraction corrected opacity profiles over the full extent of the rings at 3.6 and 13 cm- λ will subsequently be available.

INVERSION THEORY

Our objective in the analysis to follow is to show that there exists a Fresnel transform relationship between the (complex) amplitude of the observed coherent signal and the microwave transmittance of the rings (defined below). Consequently, simple analytic inversion of such transform allows reconstruction of the transmittance at a much finer resolution than would have been possible had the phase of the coherent signal not been also measured.

Geometry

The geometry of radio occultation and formulation of the received signal in terms of physical ring models have been discussed at length elsewhere (Marouf et al. 1982) and results of diffraction limited microwave opacity profiles over the full radial extent of the rings have also been published (Tyler et al., 1983). Fig. 1 gives an alternative view of the occultation geometry projected on two orthogonal planes in a Saturniocentric coordinate system. The xy-plane coincides with the mean ring plane, which is assumed to be orthogonal to the north pole of Saturn (z axis). During occultation, the spacecraft and Earth are located on opposite sides of the rings, hence the line-of-sight penetrates the ring plane at the point (x_0, y_0) , or (ρ_0, ϕ_0) if circular cylindrical coordinates are used. Azimuthal angles are referenced to the x-axis whose direction is along the Earth-Saturn vector at the time of the experiment projected on the ring plane. In Fig. 1, the angle β defines the ring opening, \hat{u}_l is a unit vector along the line-of-sight, and R_c is the spacecraft position vector; other geometric parameters are as defined by the Figure. Typical values of some geometric parameters for the Voyager 1 radio occultation experiment (November 13, 1980) are given in Table I; other entries to this Table will be introduced later.

Please note that in the actual experiment, dual-wavelength coherent signals were transmitted from the spacecraft and received on the Earth. Because it is somewhat easier to think in terms of an incident plane wave and diffracted spherical waves, the analysis here assumes the opposite configuration of the transmitter and the receiver; by reciprocity, however, identical results should be obtained for the actual experimental configuration.

Fresnel-Huygens Formulation

The reader is reminded here that because of the random positions of ring particles in space, and also because of the random intrinsic properties of the particles (e.g., size, shape, orientation,...etc.), the radio signal emerging from the rings during occultation is random in nature. This paper deals only with the coherent component of this signal, that is, the component that characterizes the average effect of ring material on the ray directly transmitted through the rings (Marouf et al., 1982). Such effect can best be described in terms of the Fresnel-Huygens principle as follows (v., e.g., Goodman, 1968).

One can think of the average effect of the ring material on the incident wave in terms of the effect of an extended planar "screen" which coincides with xy-plane in Fig. 1. Thus, for a plane harmonic wave of frequency ω , wavelength λ , and wavenumber k ($k=2\pi/\lambda$) incident along \hat{u}_i , the coherent field E_c observed at R_c may be obtained by coherent addition of the contributions of all (fictitious) secondary sources formed just behind this screen. The result is

$$E_c = \iint d\rho \left[\frac{\mu_0}{i\lambda} T(\rho) e^{ik\hat{u}_i \cdot \rho} \right] \frac{e^{ik|R_c - \rho|}}{|R_c - \rho|} \quad (1)$$

where the term in brackets represents the complex amplitude of a secondary source of infinitesimal area dp and the last term represents the spherical wave that emanates from such source to the receiver at R_c . Note that the complex amplitude is affected by: (i) the so-called "obliquity factor," which, because the occultation geometry limits observation angles to near forward directions, is assumed in Eq. (1) to be constant = $\mu_0 = \cos(\underline{B})$, (ii) the relative phase of the incident plane wave at p , represented by the term $\exp(ik\hat{u}_i \cdot p)$, and (iii) the deterministic function $T(p)$ which embodies the average amplitude and phase changes introduced by the ring particles. One can define $T(p)$, therefore, as the ratio of the complex amplitude of the secondary source formed behind the ring plane at position p in the presence and absence of the rings, respectively. We refer to $T(p)$ in this paper as the (complex) transmittance of the rings. Our objective will be to use the measurements of E_c to recover $T(p)$ from Eq. (1).

Before we proceed to accomplish such objective, we introduce the new normalized observable function \hat{T} defined as

$$\hat{T} = E_c e^{-ik\hat{u}_i \cdot R_c} \quad (2)$$

that is, the observed coherent field normalized by the incident field that would have been observed at R_c had there been no ring material along the line-of-sight. Such normalization compensates the phase of E_c for a geometric component introduced solely by the changing phase path due to spacecraft motion along its accurately known trajectory (Tyler et al., 1983). Thus both \hat{T} and T embody only effects caused by encountered ring material.

The question now is: can one reconstruct from the measurements of the complex samples of \hat{T} versus time the transmittance function $T(p)$ from Eq.

(1)? The answer depends, of course, on whether further assumptions can be made about $T(\rho)$. In general, the two dimensional function $T(\rho)$ cannot be reconstructed from measurements of \hat{T} along a single occultation track. Fortunately, however, the near circular symmetry of Saturn's rings, at least over the limited region of ring area effectively contributing to Eq. (1), renders $T(\rho)$ to be one dimensional (function of the magnitude ρ only) thus allowing for a positive answer to the above question.

1D-Screen Approximation

In a circular cylindrical coordinate system in which the screen coincides with the (ρ, ϕ) plane and $T(\rho) = T(\rho)$, Eqs. (1) and (2) combine to give

$$\hat{T} = \frac{\mu_0}{i\lambda} \int_0^{\infty} d\rho \rho T(\rho) \int_0^{2\pi} d\phi \frac{e^{ik[|R_c - \rho| - (R_c - \rho) \cdot \hat{u}_1]}}{|R_c - \rho|} \quad (3)$$

Note that when $\rho = \rho_0$, $R_c - \rho_0$ is in the direction of \hat{u}_1 (See Fig. 1) and the exponent in the ϕ -integral vanishes. At positions ρ far away from this (stationary) position, the ϕ integrand oscillates rapidly, resulting in negligible contribution to \hat{T} . The extent of the screen area that significantly contributes to \hat{T} can be found by assuming $\phi = \phi_0 + \tilde{\phi}$, where $\tilde{\phi}$ is small, and performing a perturbation expansion in powers of $\tilde{\phi}$. Details are given in the Appendix; the result when keeping only first order terms in $\tilde{\phi}$ is

$$\hat{T}(\rho_0) = \frac{1-i1}{2} \int_{-\infty}^{\infty} T(\rho) e^{i\frac{\pi}{2} \left[\frac{\rho_0 - \rho}{F} \right]^2} d\rho/F \quad (4)$$

where the characteristic dimension F (the interval $\rho - \rho_0$ for which the Kernel phase = $\pi/2$) defines the radius of an effective Fresnel zone along the

radial dimension ρ , whose value is solely determined by the occultation geometry and observation wavelength λ , namely,

$$F = \left[\frac{\lambda D}{2} \frac{c_o^2 \mu_o^2 + s_o^2}{\mu_o} \right]^{1/2} \quad (5)$$

where $D = |R_c - \rho_o|$, $\mu_o = \cos(\underline{B})$, $c_o = \cos \phi_o$, $s_o = \sin \phi_o$, and the angles \underline{B} and ϕ_o have been defined in Fig. 1. Typical values of F computed for the Voyager 1 radio occultation geometry at $\lambda = 3.6$ cm are given in Table I.

The infinite limits of the integral in Eq. (4) are, of course, only a mathematical convenience, since the actual extent of the ring material is finite in ρ . These limits allow one, however, to interpret Eq. (4) as a Fresnel transform relationship between \hat{T} and T , whose inverse can be shown to be

$$T(\rho) = \frac{1+i1}{2} \int_{-\infty}^{\infty} \hat{T}(\rho_o) e^{-i\frac{\pi}{2} \left[\frac{\rho - \rho_o}{F} \right]^2} d\rho_o / F \quad (6)$$

Thus, from the occultation geometry, the Fresnel zone F is first computed, then the measured complex samples of \hat{T} are "filtered" using Eq. (6) to reconstruct T at radial resolution much finer than F itself. An example to demonstrate the working of the theory and to motivate the discussion to follow of its limitations is in order.

Example I

Numerical computations of the inverse Fresnel transform (6) can be carried out using either one of two approaches. The first is a straightforward discretization of the integral using the measured temporal samples of \hat{T} interpolated on an equispaced grid in ρ_o , namely,

$$T_m = \frac{1+i1}{2} \sum_{n=-N/2}^{N/2} \hat{T}_{m+n} \int_{(n \pm \frac{1}{2})\Delta\rho/F} e^{-i\frac{\pi}{2} \eta^2} d\eta \quad (7)$$

where $\Delta\rho$ is the distance between samples of \hat{T} , T_m is $T(\rho = m\Delta\rho)$, m an integer, and $N\Delta\rho$ is the width of the data window (centered at $m\Delta\rho$) used to evaluate T_m . The Fresnel integrals on the right side of (7) can be computed, for example, from known series approximations (v., e.g., Boersma, J., 1960).

The second approach relies on recognizing the fact that the integral in Eq. (6) is actually a convolution integral which may be evaluated using Fast Fourier Transform (FFT) techniques. Because of its speed, the FFT approach is more convenient for systematic reduction of the large volume of data collected over the full extent of the ring system. Both approaches were used in our data reduction; with excellent agreement obtained.

Experimental details relevant to the radio occultation data reduction procedure have been discussed at length by Tyler et al. (1983) and will not be repeated here. We draw the attention of the reader, however, to the fact that \hat{T} in the analysis here is equivalent to \hat{E}_C in the notation of Tyler et al. normalized to unit amplitude in free-space.

Our first example is derived from the Voyager 1 data in the neighborhood of the Encke division, whose center is located at $\rho \approx 133,590$ km and whose width ≈ 320 km. Both edges of this division exhibit clear diffraction patterns that are characteristic of two widely separated knife edges of gray screens (Marouf and Tyler, 1982). Fig. 2a and b show the measured magnitude and phase of \hat{T} generated from independent data samples separated a distance

$\Delta\rho = 1.2$ km. Compared to a Fresnel zone radius of $F = 15.273$ km at the mean radial position of the division, this separation distance adequately samples

the first several oscillations on the clear sides of the edges. To obtain the inverse transform, Eq. (6) was used, assuming F above and a data window of width $W = N\Delta\rho = 390$ m. The magnitude and phase of the recovered transmittance $T(\rho)$ are shown in Fig. 2c and d, respectively. Note in particular the disappearance of any regular oscillation pattern in the magnitude curve, the absence of any marked overshoot of free space level, and the much sharper signal level transition at the edges. Numerical examination of sample values of the reconstructed magnitude indicate that the transition from near-zero to near-unity levels occurs over the distance of one sample at either edge, in agreement with an upper bound of about 1.5 km on edge taper projected in the ring plane obtained by model fitting studies of the same observations (Marouf and Tyler, 1982).

A first order conclusion based on the results above is that the inversion algorithm appears to work. However, several important issues remain to be examined before one can draw any quantitative conclusions from the recovered profiles. Obvious questions are: (i) does the data window width W chosen preserve the resolution of the original data points?; (ii) can the resolution be further refined so that tighter bounds on the edge taper may be obtained?; (iii) what are the limits on the resolutions achievable in other thicker parts of rings?; (iv) how sensitive is the inversion process to perturbations in F ?; (v) does any of the signal fluctuations within the apparently clear division (see Fig. 2c) correspond to a real embedded feature?; and (vi) when does the 1D-screen approximation used become invalid?

To shed more light on these important issues it is necessary to examine in some detail the systematic and random limitations of the inversion theory above. This is carried out throughout the remainder of this paper, where the above example is revisited and other examples are also considered.

SYSTEMATIC LIMITATIONS

Much like Fourier transforms, the forward and inverse Fresnel transforms (Eqs. (4) and (6)) are symmetric in form, except for the sign of i . One may think of the forward transform as an operation that distorts the actual profile $T(\rho)$ through convolution with quadratic phase factor, and of the inverse transform as the "filter" necessary to compensate exactly for such distortion, so that $T(\rho)$ may be recovered. If the inversion filter is slightly imperfect, either because a finite data window W is used and/or because F is not exactly known or vary across W , the reconstructed profile will be a somewhat distorted version of $T(\rho)$. Even in the absence of any filter imperfections, errors in $T(\rho)$ can be caused by systematic drifts in the phase of the reference oscillator used. Below, we quantify the effect of these imperfections in terms of a single parameters, namely, the radial resolution R , and examine conditions under which the simple inverse transform (6) needs extension.

In each of the cases examined, we denote by $H_{\text{SUB}}(\rho)$ the distorted profile recovered with an imperfect filter from the "data" corresponding to a hypothetical transmittance $T(\rho) = \delta(\rho)$, where $\delta(\cdot)$ is the Dirac-delta function and the subscript SUB identifies the source of the imperfection. One measure of the radial resolution R_{SUB} is the finite width of H_{SUB} , taken here to be the equivalent width of $|H_{\text{SUB}}|^2$ (v., e.g., Bracewell, 1977), namely,

$$R_{\text{SUB}} = \int_{-\infty}^{\infty} |H_{\text{SUB}}(\rho)|^2 d\rho / |H_{\text{SUB}}(0)|^2 \quad (8)$$

Our objective will be to find which of the imperfections considered sets the limit on the finest resolution achievable and determine such limits.

Finite Data Window

In principle, the diffraction pattern of any local ring feature extends indefinitely in space. Thus by limiting the extent of the data to be inverted to a finite width W , one could only hope to recover the transmittance of such feature to within some finite resolution. Think, for example, in terms of the classical diffraction pattern of an opaque knife edge. On the clear side of the edge, assumed to be at ρ_E , the period of oscillation of the magnitude of the diffraction pattern decreases with distance from the edge approximately as $2F^2/|\rho - \rho_E|$. By chopping off the pattern everywhere outside the interval $|\rho - \rho_E| \leq W/2$, all spatial frequencies of wavelength $\leq 4F^2/W$ are lost, thus when this "data" is inverted, the edge must exhibit a finite rise distance whose magnitude is of order $4F^2/W$.

As outlined above, we approach the resolution problem quantitatively by computing first the distorted profile $H_W(\rho)$ corresponding to $T(\rho) = \delta(\rho)$. Substituting this impulsive profile in Eq. (4), using the resultant $\hat{T}(\rho_0)$ back in Eq. (6), and performing the integration over the finite interval $-W/2 \leq \rho_0 \leq W/2$, one gets

$$H_W(\rho) = \left\{ \frac{W}{2F^2} \operatorname{sinc}\left(\frac{W}{2F^2} \rho\right) \right\} e^{i \frac{\pi}{2} \frac{\rho^2}{F^2}} \quad (9)$$

where $\operatorname{sinc}(x) \equiv \sin(\pi x)/\pi x$. The original impulse $T(\rho)$ and the magnitude $|H_W(\rho)|^2$ are shown in Fig. 3a and b, respectively, plotted as a function of the normalized distance ρ/F for the case $W/F = 50$. As one may expect, a finite W maps the original δ -function into a new profile which possesses a

main lobe of finite width and many other minor side lobes. The equivalent width of such a profile is obtained by substituting Eq. (9) in Eq. (8); the result is

$$R_W = 2F^2/W \quad (10)$$

a relationship that implies that the resolution can be made arbitrarily fine by simply increasing W . This is true only if the Fresnel zone F is exactly known and remains constant over W , an obvious idealization that is removed below.

Fresnel Zone Uncertainty

Substantial distortion in the shape of $H_W(\rho)$ may result if the Fresnel zone F used in the inverse transform (6) is in error by an amount δF . Generalization of Eq. (10) to include the effect of δF is carried out in the Appendix, where we show that if $|\delta F/F| \ll 1$ then Eq. (10) assumes the modified form

$$H_{\delta F}(\rho) = [C(\xi_1) - C(\xi_2) + iS(\xi_1) - iS(\xi_2)] \frac{e^{-i \frac{\pi}{2} (\frac{\rho}{\gamma F})^2}}{2\gamma F} \quad (11a)$$

where $\gamma \equiv \sqrt{2\delta F/F}$ and $C(\cdot)$ and $S(\cdot)$ denote the real and imaginary parts of the Fresnel integral (Abramowitz and Stegun, 1972, p. 300). The arguments ξ_1 and ξ_2 are given by

$$\xi_2 = \frac{\rho}{\gamma F} \pm \frac{W}{2F} \gamma \quad (11b)$$

An example that demonstrates the marked sensitivity of $|H_{\delta F}(\rho)|^2$ to errors in F is shown in Fig. 3c, where $\delta F/F = 0.3\%$ and $W/F = 50$, the same window width used in Fig. 2b where $\delta F = 0$. Note in particular the substantial distortion in the shape of the profile and the marked increase in its width for an error as small as 0.3% in F .

The radial resolution $R_{\delta F}$ corresponding to $H_{\delta F}$ can be obtained from Eqs. (8) and (11) and is shown in the Appendix to be

$$R_{\delta F} = \frac{2F^2}{W} \frac{Q^2}{C^2(Q) + S^2(Q)} \quad (12)$$

where $Q = \gamma W/2F$. In the limit $\gamma W \rightarrow 0$, Eq. (12) reduces to Eq. (10), as it should. Contrary to R_W in Eq. (10), however, $R_{\delta F}$ increases linearly with W in the limit $W \rightarrow \infty$. Salient characteristics of $R_{\delta F}$ are displayed by the solid curve in Fig. 4, where $R_{\delta F}/\gamma F$ is plotted versus Q . The dashed lines represent the asymptotes $\gamma W \rightarrow 0$ and $\gamma W \rightarrow \infty$. The optimal resolution is achieved when $Q \approx 1$, that is, when the width of the data window is

$$W_{\delta F} = 2F/\gamma \quad (13)$$

and has a value

$$R_{\delta F} = 2.5 F^2/W_{\delta F} = 1.25 \gamma F \quad (14)$$

which is 25% larger than the $\delta F = 0$ value obtained from (10) for the same window width.

Eq. (14) implies that to achieve a sub-kilometer resolution ($R_{\delta F} < 10^3$ m) in regions where F is 9-15 km (Table I) requires γ to be

$\lesssim 0.05$, or $|\delta F/F| \lesssim 0.14\%$; sub-hundred meter resolution, on the other hand, requires that $|\delta F/F| \lesssim 0.0014\%$

This marked sensitivity of resolution to errors in F immediately prompts the question: How accurate can F be estimated from the geometry of the radio occultation experiment? As one may see from Eq. (5) for F , the answer depends on the accuracy in knowledge of the geometric parameters D , ϕ_0 , and μ_0 . Such parameters are affected by uncertainties in knowledge of the direction of Saturn's pole vector and also by timing uncertainties in the position vector of the spacecraft along its trajectory. These uncertainties primarily translate into an error δp_0 in determination of the radius of intersection p_0 (Fig. 1), from which δF can be approximately estimated to be $\delta F = F' \delta p_0$, where $F' = \partial F / \partial p_0$ evaluated at the nominal point of intersection.

Utilizing the different viewing geometries of the radio and ultraviolet Voyager occultation experiments to correct for the offset in the radial locations of several prominent ring features, Simpson et al. (1983) report corrections to the direction of Saturn's pole that constrain δp_0 to be well within 10 km. Conservative bounds on $|\delta F/F|$ in different regions of the rings can thus be obtained from the slopes F' listed in Table I using $|\delta p_0| \leq 10$ km; such bounds were used to compute the values of γ given in Table I. Corresponding optimal resolutions and window widths can be computed from Eqs. (11) and (13), respectively, and are given in Table II, where $R_{\delta F}$ varies from a few hundred meters in inner ring C to a few tens of meters in the neighborhood of ring F. Whether these resolutions are achievable or not depends on the limitations imposed by the additional imperfections discussed below.

Finite Curvature

One idealization in deriving the inverse transform (6) is the assumption of a constant Fresnel zone F . Two effects combine to violate this assumption: The first is the time changing occultation geometry which causes F to vary with ρ_0 , as the finite, yet small, derivative F' in Table I indicates; the second is not as obvious, and is caused by the finite curvature of the assumed circular contours of $T(\rho)$. The analysis below shows the second effect to be dominant for the Voyager geometry.

An alternative approach to derive the forward transform (4) is to approximate $T(\rho)$ at any observation point ρ_0 by a new function which assumes constant values along straight lines tangent to the contours of $T(\rho)$ and perpendicular to ρ_0 . As the width W increases to accomodate the resolutions, this straight-contours approximation becomes less valid and Eq. (4) must be extended to incorporate at least first order effects of the finite curvature.

Recall that Eq. (4) was obtained from the general form (3) through the assumption that over the ring area effectively contributing to the coherent signal the angle ϕ deviates a small amount $\tilde{\phi}$ from ϕ_0 , so that a perturbation expansion in $\tilde{\phi}$ leads to Eq. (4) if only first order terms in $\tilde{\phi}$ are kept. This approach allows one to extend Eq. (4) to include the first order effects of curvature through incorporation of terms upto second order in $\tilde{\phi}$ in the perturbation expansion. In the Appendix, we show that the dominant effect of the additional terms in $\tilde{\phi}$ is to modify Eq. (4) to the new form

$$\hat{T}(\rho_0) = \frac{1-i1}{2} \int_{-\infty}^{\infty} T(\rho) e^{i \frac{\pi}{2} \left[\frac{\rho_0 - \rho}{F} \right]^2 \left[1 - \frac{2F'}{F} (\rho - \rho_0) \right]} d\rho / F \quad (15)$$

where F'_c is a dimensionless quantity that plays the same role as a partial derivative of F with respect to ρ evaluated at the point of observation ρ_0 . Its magnitude is inversely proportional to the radius of curvature and is given by

$$F'_c = \frac{F}{2\rho_0} (\mu_c - \mu_0^{-1})^2 c_0^2 s_0^2 \frac{c_0^2 \mu_0^2 + s_0^2}{s_0^2 \mu_0^2 + c_0^2} \quad (16)$$

where the geometric parameters μ_0 , c_0 , and s_0 have been previously defined. Table I gives typical values of F'_c for the Voyager geometry, computed from Eq. (16) using table I entries for F , ϕ_0 , and ρ_0 . Note that F'_c as defined by Eq. (16) is always positive.

Contrary to the forward transform (4), the modified transform (15) does not seem to possess an exact analytic inverse similar to Eq. (6). One is tempted, however, to still adopt the symmetric form

$$\tilde{T}(\rho) = \frac{1+i1}{2} \int_{\rho \pm W/2} \hat{T}(\rho_0) e^{-i \frac{\pi}{2} \left[\frac{\rho - \rho_0}{F} \right]^2 \left[1 - \frac{2F'_c}{F} (\rho - \rho_0) \right]} d\rho_0 / F \quad (17)$$

as an approximate inverse of Eq. (15). Clearly, $\tilde{T}(\rho)$ will differ from the original profile $T(\rho)$, and such difference will set an additional limit on achievable resolution. Before we compute such limit, it is instructive to examine first the additional effect of the geometric change in F .

Generalization of Eqs. (15) and (17) to incorporate the geometric change in F is heuristically obtained by substituting the variable Fresnel zone $F(\rho_0)$ for F . For the Voyager geometry, the drift in F with ρ_0 is dominated by a linear component and can be locally approximated by the first order Taylor expansion

$$F(\rho_0) = F(\rho) + (\rho_0 - \rho)F' \quad (18)$$

where typical values of F' are given in Table I. If, in addition, the relative perturbation in F is small (i.e., if $\left| \frac{W}{2} \frac{F'}{F} \right| \ll 1$), then only the first order perturbation in the phase of the Kernel of Eq. (17) is of importance, giving

$$\tilde{T}(\rho) = \frac{1+i1}{2} \int_{\rho \pm W/2} \hat{T}(\rho_0) e^{-i \frac{\pi}{2} \left[\frac{\rho - \rho_0}{F} \right]^2 \left[1 - \frac{2(F'_C - F')}{F} (\rho - \rho_0) \right]} d\rho_0/F \quad (19)$$

as the modified approximate transform that compensates for both geometric and curvature-caused drifts in F , where F now actually stands for $F(\rho)$.

Interestingly, since F' and F'_C are of the same sign (see Table I), their effects in Eq. (19) act to cancel one another. Unfortunately, however, their magnitudes greatly differ, with the effect of F'_C being the dominant one. Thus, in the following discussion of resolution we limit our attention to Eqs. (15) and (17) only.

As before, we obtain the resolution from the profile $\tilde{T}(\rho) = H_C(\rho)$ corresponding to $T(\rho) = \delta(\rho - \rho^*)$, where the subscript C stands for curvature. Contrary to the assumption $\rho^* = 0$ before, ρ^* here is assumed large so as to avoid a fictitious singularity in F'_C since ρ_0 assumes values of the same order as ρ^* (see Eq. (16)). The profile H_C is then obtained by substituting Eq. (15) back into Eq. (17) and performing the resultant integration. The result (for $\left| \frac{W}{2} \frac{F'_C}{F} \right| \ll 1$) is exactly similar to Eq. (11) except that the constant γ in that equation is now replaced by the ρ -dependent term $[6F'_C(\rho - \rho^*)/F]^{1/2}$. The corresponding equivalent width is obtained from Eq. (8) and is shown in the Appendix to be

$$R_C = \frac{2F^2}{W} \left[\frac{1}{2U} \ln\left(\frac{1+U}{1-U}\right) \right] \quad (20)$$

where $U \equiv 3F'_C W/F$ and is assumed to be < 1 . Thus, in the limit $F'_C \rightarrow 0$ (i.e., $U \rightarrow 0$), Eq. (20) reduces to Eq. (10), while in the limit $U \rightarrow 1$, R_C increases indefinitely (probably an artifact of the violation of the initial assumption $|F'_C W/2F| \ll 1$). A minimum of R_C is reached at $U \approx 0.8$, as illustrated by the dash-dot curve in Fig. 4, where $R_C/3F'_C F$ is plotted versus U . The corresponding optimal width W_C and resolution R_C are given by

$$W_C \approx 0.27 F/F'_C \quad (21)$$

and

$$R_C \approx 2.75 F^2/W_C = 10.30 F'_C F \quad (22)$$

A comparison of values of R_C and W_C to $R_{\delta F}$ and $W_{\delta F}$ is given in Table II. Clearly, W_C and $W_{\delta F}$ are comparable in ring C, both limiting the resolution to few hundred meters. The two widths systematically diverge, however, with increasing distance from Saturn, with W_C becoming the dominant limiting factor, where it limits resolution to about 100 meters in outer ring A and in the neighborhood of ring F.

Oscillator Phase Drift

Recall that the inverse transform (6), or its modified form (17), requires full knowledge of the amplitude and phase of the measured signal $\hat{I}(\rho_0)$. The phase measurement is actually a relative measurement, referenced to the phase of a coherent sinusoidal signal generated onboard the spacecraft from a highly stable, radiation hardened, quartz oscillator (Eshleman et al.,

1977). The radio occultation measurements were preprocessed so as to compensate for large scale systematic drifts in the estimated frequency of this oscillator (Tyler et al., 1983). Nonetheless, a residual phase error $\phi_r(\rho_0)$ may persist over the width of the data window used and the effect of these residuals on the inversion is assessed here.

Consider the inverse transform (6) in the presence of slowly drifting residual phase $\phi_r(\rho_0)$ contaminating the phase measurements of $\hat{T}(\rho_0)$. Assuming that ϕ_r may adequately be approximated by the first three terms of its Taylor series expansion about the center ρ of the data window, i.e., $\phi_r(\rho_0) = \phi_r(\rho) + \phi_r'(\rho_0 - \rho) + 0.5 \phi_r''(\rho_0 - \rho)^2$, the perturbed inverse transform becomes

$$\tilde{T}(\rho) = \frac{1+i1}{2} e^{i\phi_r(\rho)-i\phi_r'(\rho)} \int \hat{T}(\rho_0) e^{i\phi_r'\rho_0-i\frac{\pi(\rho-\rho_0)^2}{2F^2}[1-\phi_r'F^2/\pi]} d\rho_0/F \quad (23)$$

It is easier to assess the effect of each of the expansion terms of $\phi_r(\rho_0)$ separately. Clearly, the first term $\phi_r(\rho)$ is a simple multiplicative constant. In the absence of ϕ_r'' , the linear phase drift in (23) introduces a linear shift in $\tilde{T}(\rho)$, whose value can be calculated by substituting in (23) the profile $\hat{T}(\rho_0)$ corresponding to $T(\rho) = \delta(\rho)$. The result is

$$\tilde{T}(\rho) = \delta[\rho + \phi_r'F^2/\pi] e^{i(\phi_r'F)^2/2\pi} \quad (24)$$

Thus, ϕ_r' primarily introduces a shift $= -\phi_r'F^2/\pi$ in the radial positions of the recovered profile. On the other hand, in the absence of ϕ_r' , the ϕ_r'' term in Eq. (23) mimics the presence of an error δF of magnitude

$$\delta F/F = \phi_r''F^2/2\pi, \text{ whose effect is to distort the recovered profile, as}$$

discussed before. In general, a combination of shift and distortion would be expected.

Estimates of ϕ_r' and ϕ_r'' for Voyager radio occultation were obtained from polynomial least-mean-square fit to the residual phase measured in free-space before and after Voyager was occulted by the rings. Several data windows of typical width in the range specified by Table II were used, leading to the bound $|\phi_r'| \lesssim 10^{-3}$ rad/km, that is, a radial shift uncertainty $\lesssim 70$ meters for $F = 9$ to 15 km. Estimates of ϕ_r'' fall in the range $|\phi_r''| \lesssim \text{rad/km}^2$, or an apparant error $\delta F/F \lesssim$, which has insignificant effect on values of γ listed in Table I. One can conclude therefore that for Voyager conditions at Saturn residual oscillator drift have little effect on resolution and mainly introduce uncertainty in the radial position of value less than several tens of meters.

Example I Revisited

A comment about the resolution of the inverted profiles of Example I above is in order. For that example, $F = 15.273$ km at $\rho = 133,590$ km; other relevent parameters are: $W = 390$ km, $F' \approx 1.6 \times 10^{-5}$, $\gamma \approx 0.0047$, $F_C' \approx 7.4 \times 10^{-4}$. Using these parameters in (13) and (21), one obtains $W_{\delta F} = 6500$ km and $W_C = 5573$ km. The last value sets the limit on achievable resolution to $R_C = 116$ m. Because $W \ll W_C$, the resolution corresponding to W used is given by Eq. (10) to be $R_W \approx 1.2$ km, which is actually the distance $\Delta\rho_0$ used to sample the initial diffraction limited data in Figs. 2a and b. Clearly, ample room for further improvement in resolution remains. The example is considered again at the end of next section.

RANDOM LIMITATIONS

Thus far, our analysis has assumed that both $\hat{T}(\rho_0)$ and its inverse $T(\rho)$ to be noise free. In fact, the actual measurement is random signal $\hat{X}(\rho_0)$ which differs from $\hat{T}(\rho_0)$ because of the contribution of noise. We shall use the notation $\hat{X} = \hat{T} + \hat{n}$ and $X = T + n$ to denote the noisy measured and reconstructed profiles, respectively, where \hat{n} and n denote the corresponding additive noise components. Because of the random nature of X , the desired profile T will never be exactly known, and it is our objective in this section to define (for any given X) a confidence interval within which the real and imaginary components of T fall with some a priori specified probability. The tradeoff between the width of these confidence intervals and resolution is examined and demonstrated with an example.

Our results will be formulated in terms of the opacity τ and the coherent phase shift ϕ_c , defined in terms of the real, X_R , imaginary, X_I , and magnitude, X_M , components of X by the two equations

$$\tau = -2\mu_0 \ln X_M \quad (25)$$

and

$$\phi_c = \tan^{-1}[X_R/X_I] \quad (26)$$

Both τ and ϕ_c relate directly to the parameters of the physical model assumed for the rings (Marouf et al., 1982). We emphasize here again that τ and ϕ_c as given by Eqs. (25) and (26) are only statistical estimates of

their exact (unknown) values τ^* and ϕ_c^* (obtained by replacing all X 's by T 's in the previous two equations). Confidence intervals for τ and ϕ_c are obtained from the corresponding confidence "region" for T_R and T_I .

Noise Model

The dominant contribution to the additive noise component \hat{n} comes from thermal noise generated at the front end of the Earth-based receiving station (Eshleman et al., 1977). The two quadrature components of this noise may be adequately modeled by uncorrelated band-limited (bandwidth = B) gaussian random functions with zero means and identical autocorrelation functions, with the total noise power P_N equally divided among the two components.

To obtain estimates of the noise power P_N we used the complex samples of the coherent signal measured in a bandwidth $B = 18750$ Hz during time periods before and after Voyager 1 was occulted by the rings. These "free space" samples were then used to compute estimates of the mean and variance over equal time intervals T_A . After normalizing the mean value to unity (as required by our definition of transmittance), the sum of the variances of the two quadrature components was taken to be the desired estimate of P_N . The results slightly fluctuate around the estimate

$$\hat{P}_N = \frac{10^{-b}}{T_A} = 10^{-b} \frac{\dot{\rho}_0}{\Delta \rho_0} \quad (27)$$

where $b = 5.02$ and 3.55 for the 3.6 and 13 cm wavelength signals, respectively, and the second equality expresses T_A in terms of the radial distance $\Delta \rho_0$ traveled in the ring plane and the radial velocity component $\dot{\rho}_0$, a convenient representation for later use. Clearly, we assume $\dot{\rho}_0$ to be nearly constant over the period T_A .

In all calculations to follow we assume P_N to be a known quantity whose magnitude is given by the estimate \hat{P}_N of Eq. (27). A check of the accuracy of such assumption may be obtained from the following formula for the normalized mean square error in \hat{P}_N (Bendat and Piersol, 1971, p. 176)

$$\frac{\text{Var}[\hat{P}_N]}{\hat{P}_N^2} = \frac{1}{BT_A} \quad (28)$$

Thus, for example, for $\Delta\rho_0 \geq 100$ m and $\rho_0^\circ = 60\text{-}80$ km/s (see Table I), $T_A \lesssim 1.25$ ms, which when used in Eq. (27), together with $B = 18750$ Hz, gives the error in P_N to be less than about 20%; for $\Delta\rho_0 \geq 1$ km, on the other hand, the error is less than about 7%.

We have also carried out numerical evaluations of the signal variance during occultation by several regions of the rings. Such variance presumably include contributions from the scattered signal which, as far as the coherent signal is concerned, constitutes an additional gaussian noise component. For all integration times considered ($\leq T_A \leq$ s), the scattered signal contribution to \hat{P}_N was negligible and was certainly within the uncertainty expressed by Eq. (28).

Note that the statistical characterization described above applies to the noise \hat{n} before being processed through the inverse Fresnel transform (6). The linearity of the transform preserves the gaussian nature of the noise, and one can show that the quadrature components of the resultant noise n remain uncorrelated and carry equal shares of the total noise power. The noise power is the same as \hat{P}_N in Eq. (27) provided that the window width is chosen so that $\Delta\rho_0 = R_W$, i.e., $W = 2F^2/\Delta\rho_0$ (c.f., Eq. (10)).

One noise component not included in our model is the random fluctuations in the phase of the reference oscillator, which introduces multiplicative

noise. Although presumed to be negligible, further analysis is needed to confirm such assumption.

Confidence Intervals

With measurement noise now included, consider the complex plane whose orthogonal axes are the unknown variables T_R and T_I (see Fig. 5). A given pair (X_R, X_I) , obtained from the inverse transform, is represented by a point in this plane which, because of the noise, is located at a position that differs from the actual pair (T_R, T_I) . One cannot locate (T_R, T_I) exactly, but can inquire in a statistical sense about the region in this plane that contains (T_R, T_I) with some specified probability given knowledge of (X_R, X_I) . This is a classical problem in statistical inference (v.,e.g., ?), whose answer is obtained by noting that the random variable C , defined by the equation,

$$C = 2[(X_R - T_R)^2 + (X_I - T_I)^2]/P_N \quad (29)$$

has a χ^2 -distribution of 2 degrees of freedom. For a given (X_R, X_I) , Eq. (29) describes circles in the (T_R, T_I) plane whose peripheries are contours of constant values of C . The particular circle that contains the pair (T_R, T_I) within it with some chosen probability $(1 - \alpha)$ defines the so called $(1 - \alpha)\%$ confidence region. The radius of such circle is $\sqrt{P_N C_\alpha / 2}$, where C_α is the value of C such that $\text{Prob}[C > C_\alpha] = \alpha$. Tables of the cumulative χ^2 -distribution gives C_α for the 50, 90, and 95% confidence regions to be 1.39, 4.61, and 5.99, respectively. Clearly, the region becomes larger as higher confidence is desired and/or as the noise power P_N increases.

From Fig. 5, one may also directly infer $(1 - \alpha)\%$ confidence intervals for τ and ϕ_c using the dashed contours tangent to the circle in that figure. Our results will be expressed in terms a "threshold opacity" τ_{TH} , defined as

$$\tau_{TH} = -\mu_0 \ln[P_N C_\alpha / 2] \quad (30)$$

which corresponds to the threshold case when the radius of the circle in Fig. 5 is such that the origin point is located on the circle's periphery. For a measured pair (τ, ϕ_c) , the $(1 - \alpha)\%$ confidence intervals that simultaneously contain the actual pair (τ^*, ϕ_c^*) can be shown to be $\tau_L \leq \tau^* \leq \tau_U$ and $|\phi_c - \phi_c^*| \leq \Delta\phi_c$, where

$$\tau_L = \tau_{TH} - 2\mu_0 \ln[e^{-(\tau - \tau_{TH})/2\mu_0} + 1] \quad 0 < \tau < \infty \quad (31a)$$

$$\tau_U = \tau_{TH} - 2\mu_0 \ln[e^{-(\tau - \tau_{TH})/2\mu_0} - 1] \quad \begin{matrix} 0 < \tau < \tau_{TH} \\ \tau > \tau_{TH} \end{matrix} \quad (31b)$$

$$\Delta\phi_c = \sin^{-1}[e^{(\tau - \tau_{TH})/2\mu_0}] \quad \begin{matrix} 0 < \tau < \tau_{TH} \\ \tau > \tau_{TH} \end{matrix} \quad (32)$$

Measured values of τ close to or greater than τ_{TH} correspond to situations in which the phase has little or no meaning and only a lower bound on the actual opacity τ^* can be established.

As obvious from Eqs. (30) and (27), factors affecting τ_{TH} are the occultation geometry (μ_0, ρ_0^*) , the desired resolution $(\Delta\rho_0)$, and the chosen confidence level (C_α) . For Voyager 1 geometry ($\mu_0 = 0.103$, and ρ_0^* in Table

I), Fig. 6 shows variation of τ_{TH} with resolution $R_W (R_W = \Delta\rho_0)$ for the two case $\alpha = 0.5$ and 0.1 (50 and 90% confidence); solid lines correspond to ρ_0^* in inner ring C while dashed lines correspond to outer ring A. Plots for the 3.6 and 13 cm wavelengths are shown. Note the degradation in values of τ_{TH} at the longer wavelength, mainly because of approximately 15 dB free-space SNR difference between the two signals.

Fig. 7 shows an example of the variations in the uncertainty intervals with measured opacity τ and data processing resolution R_W . The example corresponds to the choices $\alpha = 0.5$ ($C_\alpha = 1.39$), $\rho_0^* = 83$ km/s (outer ring A), and $\lambda = 3.6$ cm. Similar families of curves for other choices can be generated from the results above. The intersection of a vertical line drawn at a measured opacity τ with the curves labeled by the same resolution number give $\Delta\phi_c$ (in cycles) from the upper set of curves and τ_L and τ_U from the lower ones. Note, for any given resolution, the rapid divergence in the width of the τ -confidence interval as τ approaches τ_{TH} and the "tightening" of the interval and increase in τ_{TH} as resolution is degraded.

In the light of the above results, a comment about the resolution limits in Table II is in order. Because these limits were derived assuming unlimited SNR, they clearly apply only to regions whose opacity τ is small compared to the corresponding τ_{TH} . If, on the other hand, τ is close to or larger than τ_{TH} , the confidence intervals become intolerably large to allow any meaningful quantitative interpretation of τ and ϕ_c . To narrow down the uncertainty, one is forced to perform coherent data averaging over longer intervals $\Delta\rho_0$ in order to reduce P_N , hence increase τ_{TH} . The price paid, of course, is degradation of resolution. As obvious from the 3.6 cm- λ curves in Fig. 6, τ_{TH} for the Voyager 1 geometry is less than about 0.8 for $\Delta\rho_0 \lesssim 1$ km, mainly because of nearly closed rings at the time of occultation

($B = 5.92^\circ$). Thus, over a good fraction of the rings, the resolution will be noise limited. One must keep in mind, however, that this conclusion applies only to the particular geometry of Voyager 1 at Saturn. To highlight this point, we show in Fig. 6 values of τ_{TH} corresponding to a hypothetical Voyager-like occultation experiment with the rings assumed to be fully open ($B = 27^\circ$; the vertical scale on the right side of Fig. 6). A 100 meter resolution nearly everywhere within the rings (radio opacity $\lesssim 1.5$) is certainly within the realm of such experiment. A nearly ideal target in that regard is, of course, the nearly fully open ($B = 90^\circ$) Uranian rings, expected to be occulted by Voyager 1 in January 1986.

To be Completed

Example I Revisited

To illustrate: sharpness of the inner edge of the Encke Division at 100 m resolution; implications for edge thickness; detached ringlets within the gap; wave phenomena interior to the inner edge.

Other Possible Examples to Choose From

Example II - Ring F

To illustrate: Why 100m resolution is necessary for narrow features (bifurcation of ring F); implications for rings of Uranus.

Example III - Mimas 5:3 Density and Bending Waves

To illustrate: Phenomenon masked by diffraction and revealed by the inversion.

Example IV - A condensation in ring C

To illustrate: utility of recovered phase & opacity at two observation wavelengths.

Example V - Maxwell's Gap (ring C)

To illustrate: sharpness of edges of embedded ringlets; fuzziness of edges of the mother gap; tradeoff between resolution and SNR.

Example VI - Some Gaps in Cassini Division

To illustrate: sharp outer edges; diffused inner edges; similarities among two gaps; possible wave phenomena next to a gap.

CONCLUSIONS

APPENDIX

REFERENCES

TABLE I
Selected Geometric Parameters

Approximate Location	Event time ^a hr:min:sec	p_0 (R_s)	ϕ_0^c (deg)	D^d (km)	F^e (km)	$F \cdot f$ $\times 10^5$	$F \cdot g$ $\times 10^4$	γ^h $\times 10^2$
Inner ring C	04:44:00	1.2342	74460	65.41	280219	9.23271	36.143	37.125
Mid ring C	04:46:34	1.3797	83236	56.14	268120	11.63250	20.694	31.294
Inner ring B	04:48:48	1.5252	92017	51.32	257587	13.07336	12.932	24.006
Mid ring B	04:51:45	1.7366	104771	45.23	243666	14.29033	6.848	15.902
Outer ring B	04:54:30	1.9476	117497	40.78	230681	14.92821	3.489	10.683
Inner ring A	04:55:28	2.0241	122114	39.44	226115	15.06855	2.629	9.304
Mid ring A	04:56:58	2.1448	129398	37.55	219028	15.21767	1.522	7.536
Outer ring A	04:58:27	2.2663	136723	35.88	212018	15.29541	0.642	6.150
Near ring F	04:59:13	2.1297	140551	35.08	208395	15.31222	0.252	5.549
Other Parameters								
Light-time, Voyager 1 to Earth				5086.6 sec				
Angle of ring opening α				5.92°				

- ^a UTC at Earth receiving station Nov. 13, 1980
^b Radial distances in the ring plane. Saturn's pole vector used is: RA = 38.409° and DEC = 83.324°.
^c Azimuth measured counterclockwise from projection of Earth-Saturn vector at the time of the experiment on the ring plane.
^d Distance from spacecraft to ring plane along occultation ray
^e Fresnel zone at 3.6 cm wavelength
^f Radial rate of change of the Fresnel zone.
^g An apparent radial change in F due to curvature of rings (see text).
^h A dimensionless parameter that characterizes errors in F (see text).

TABLE II

Resolution Limits and Corresponding Data Window Width

Approximate ^a Location	$R_{\Delta F}$ (m)	$(/F)^b$	$W_{\Delta F}$ (km)	$(/F)$	R_C (m)	$(/F)$	W_C (km)	$(/F)$
Inner ring C	323	0.0350	660	72	353	0.0382	671	73
Mid ring C	273	0.0236	1237	106	375	0.0322	1004	86
Inner ring B	230	0.0176	1858	142	323	0.0247	1470	113
Mid ring B	175	0.0133	2919	204	234	0.0164	2426	170
Outer ring B	128	0.0085	4365	292	164	0.0110	3773	253
Inner ring A	111	0.0074	5099	338	144	0.0096	4373	290
Mid ring A	85	0.0056	6808	447	118	0.0078	5452	358
Outer ring A	55	0.0036	10549	700	97	0.0063	6715	479
Near ring F	35	0.0023	16920	1105	88	0.0056	7451	497

^a Radial positions are given in Table I.^b Quantity measured in units of Fresnel zone F, where F is given in Table I.ORIGINAL PAGE IS
OF POOR QUALITY

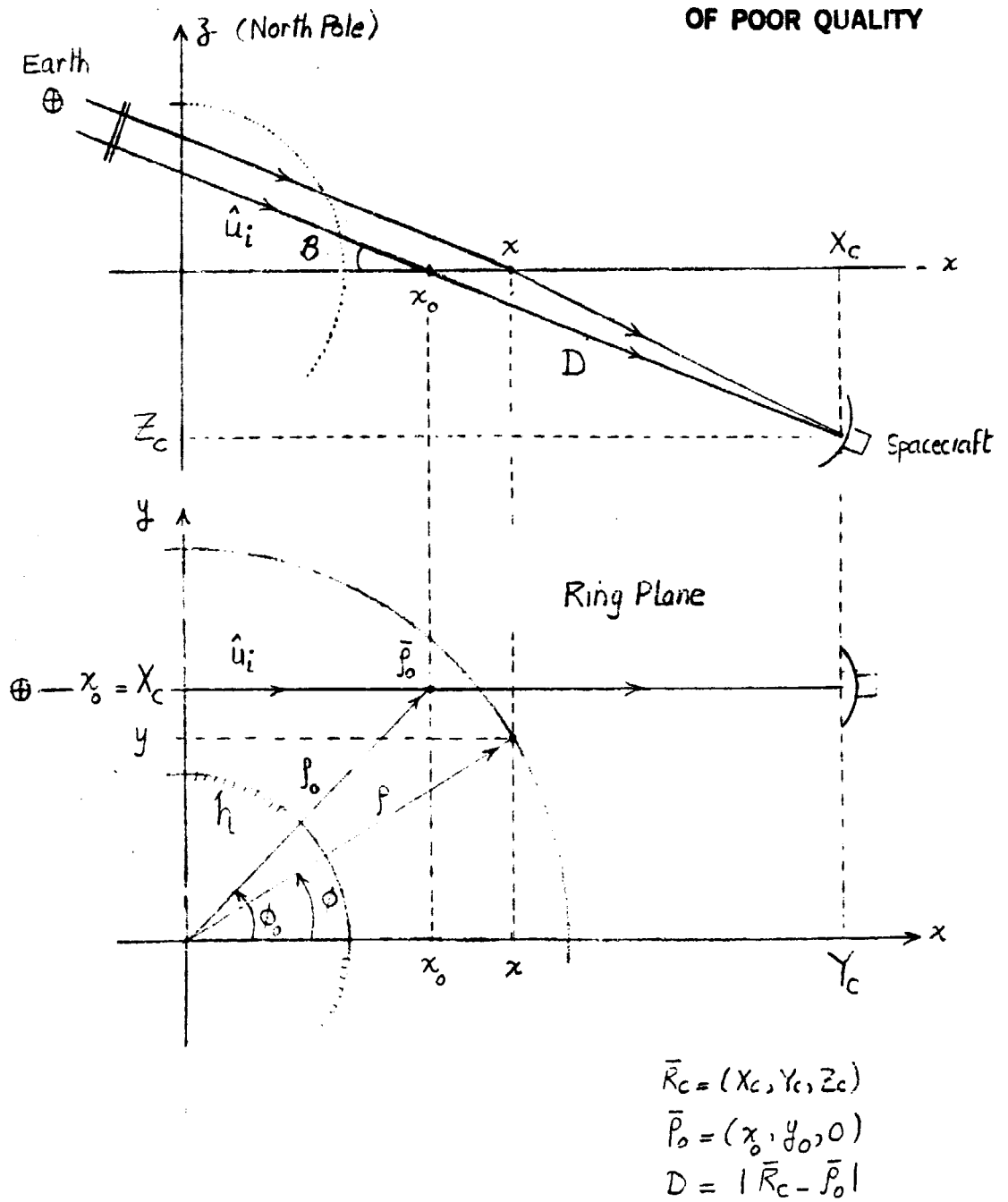
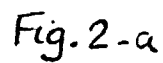


Fig. 1 Geometry of radio occultation in a Saturn-centric Coordinate System.

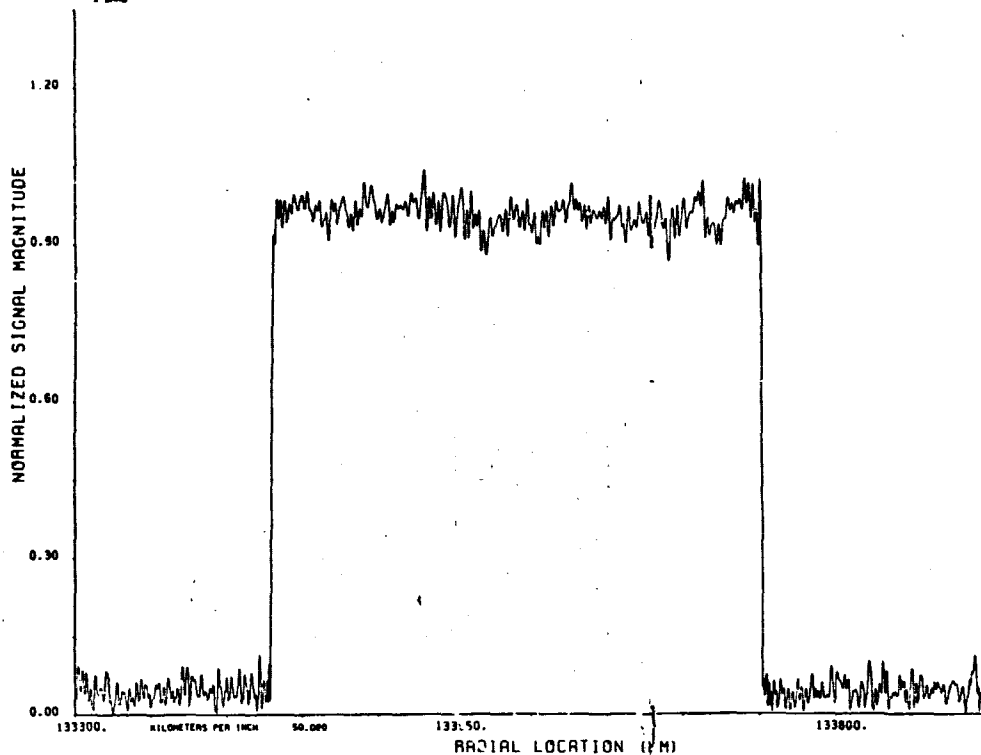
```
FILE NAME      DMS:C2SCATCH.PAN3XBRND.POL:111
DATE           2-SEP-83                               TIME      18:53:18

DATA PT. SPACING MM 250.0
A BRND
```



ORIGINAL PAGE 18
OF POOR QUALITY

FILE NAME DISKUSER1:CPAUL.SATURN.INVERSION\INVERSION.OUT:1
DATE 2-SEP-83 TIME 15:46:20
INVER. RESOLUTION MM 1200.0 PLOT RESOLUTION MM 1200.0
DATA PT. SPACING MM 250.0
X BAND



FILE NAME DISKUSER1:CPAUL.SATURN.INVERSION\INVERSION.OUT:1
DATE 2-SEP-83 TIME 17:41:57
INVER. RESOLUTION MM 1200.0 PLOT RESOLUTION MM 1200.0
DATA PT. SPACING MM 250.0
X BAND

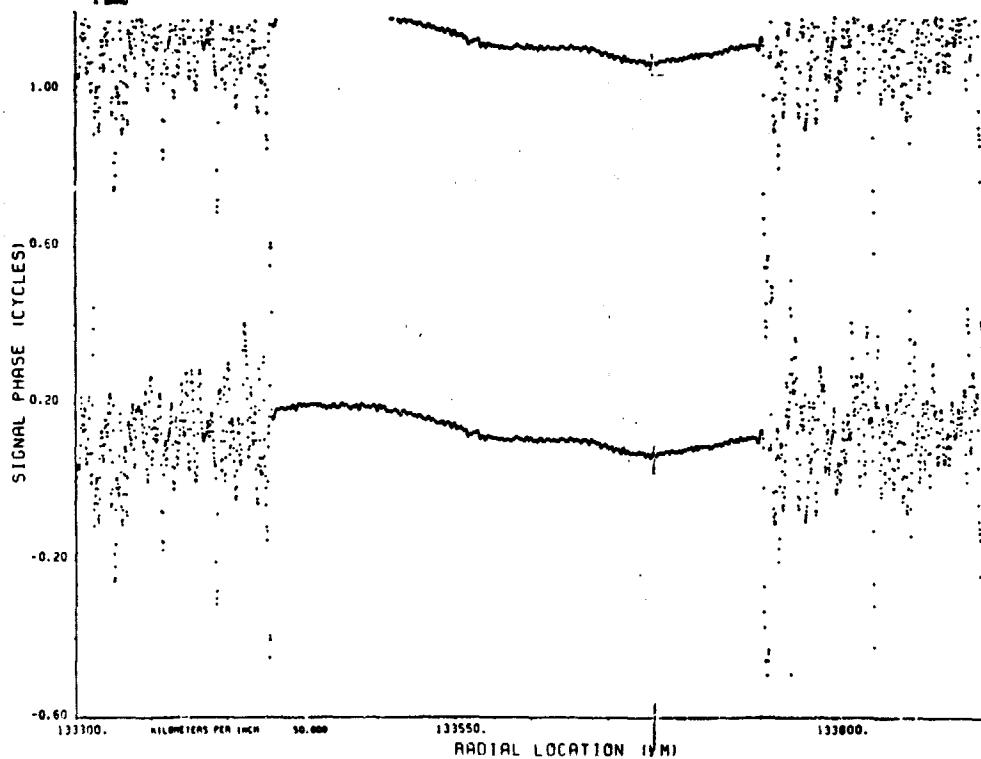
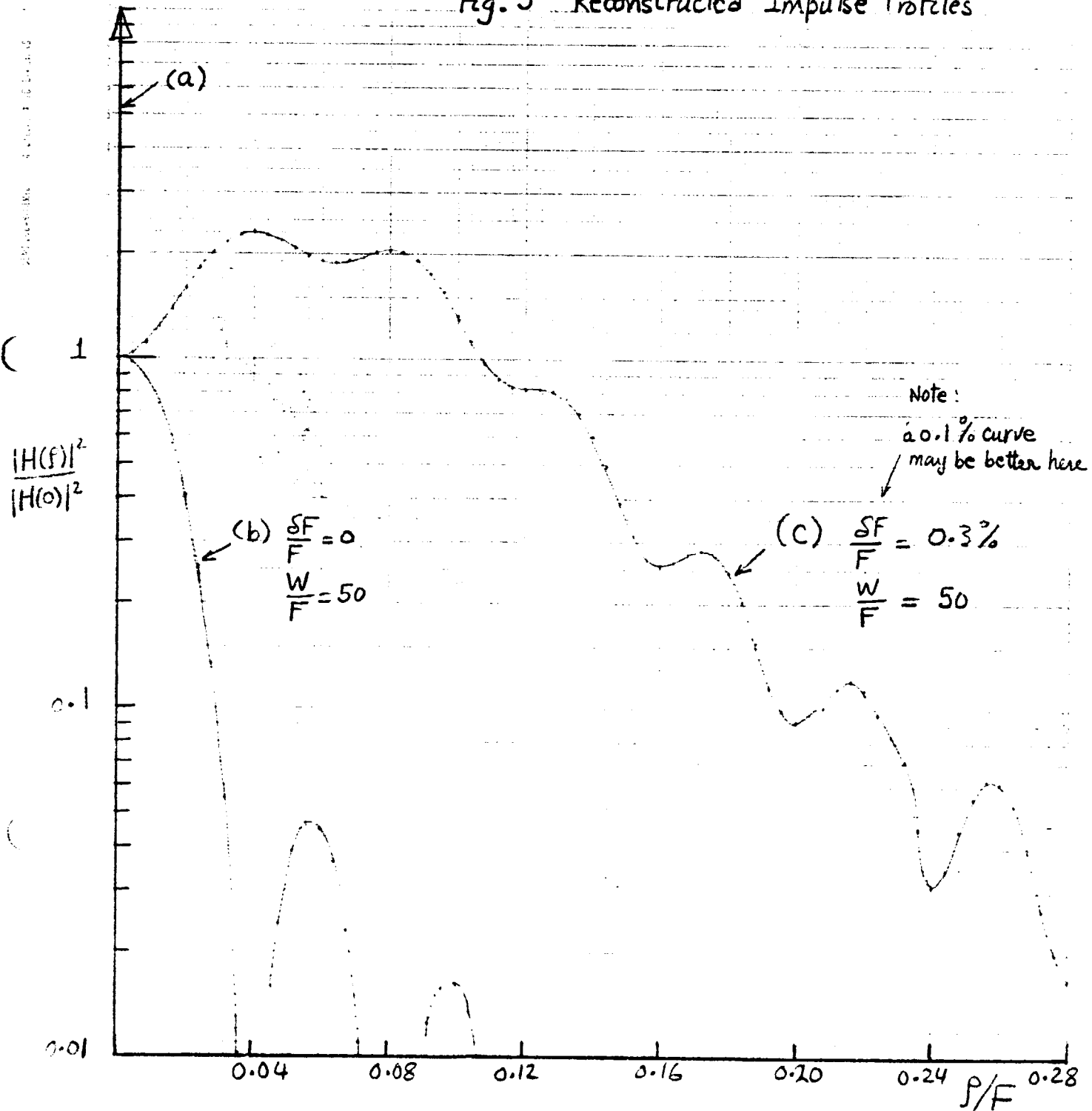


Fig. 3 Reconstructed Impulse Profiles



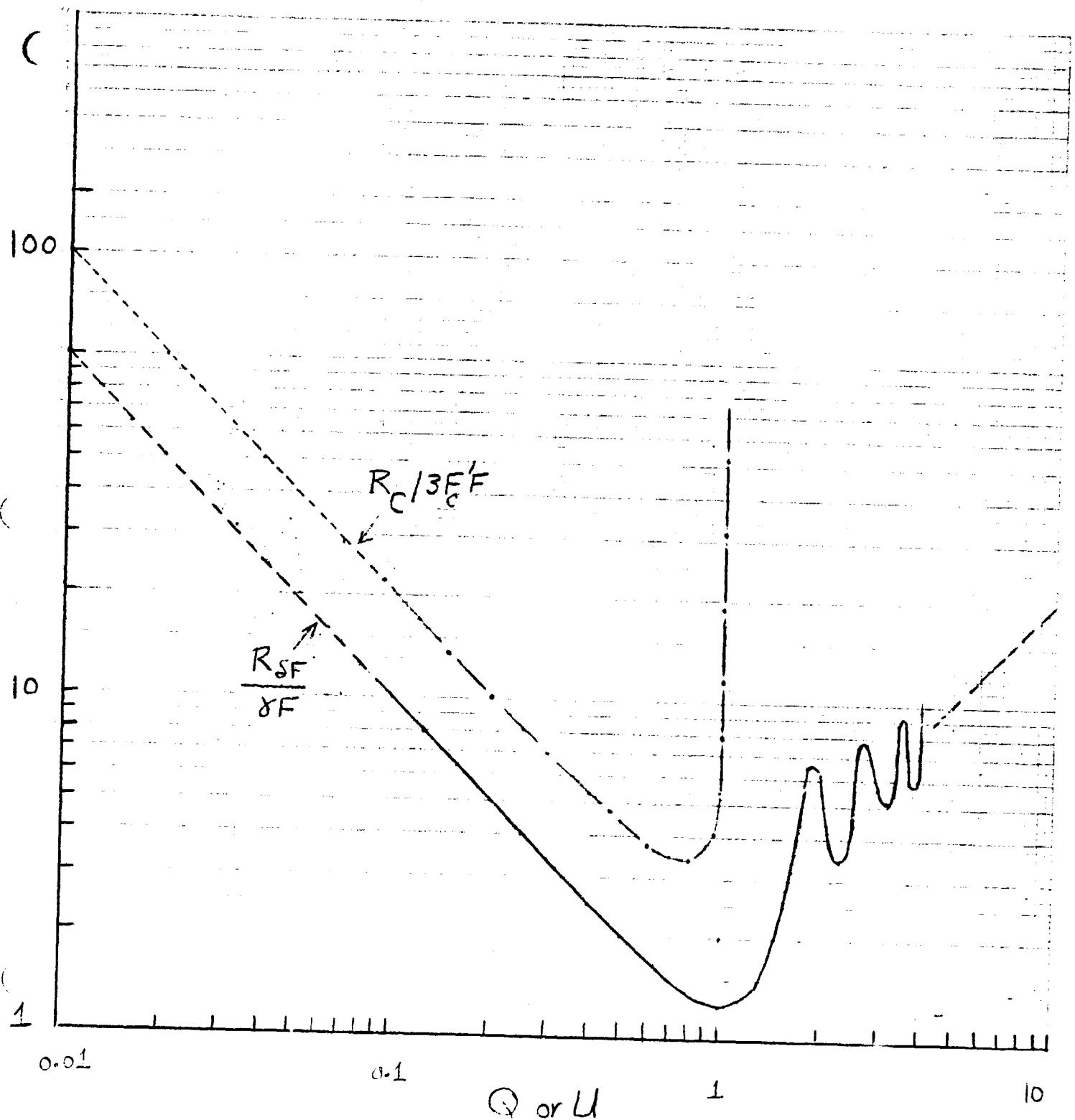


Fig. 4 Variation of Resolution With Window Width

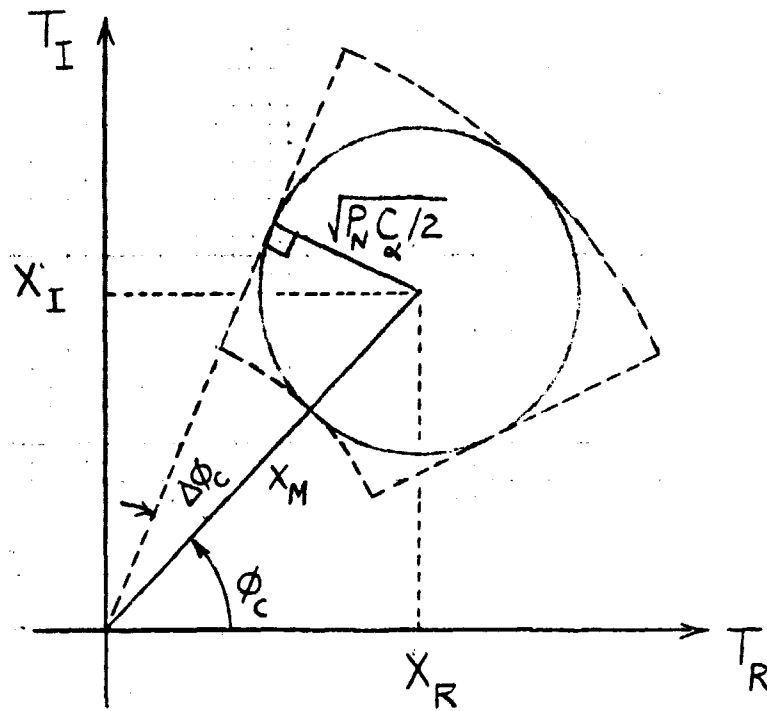


Fig. 5 Confidence Region

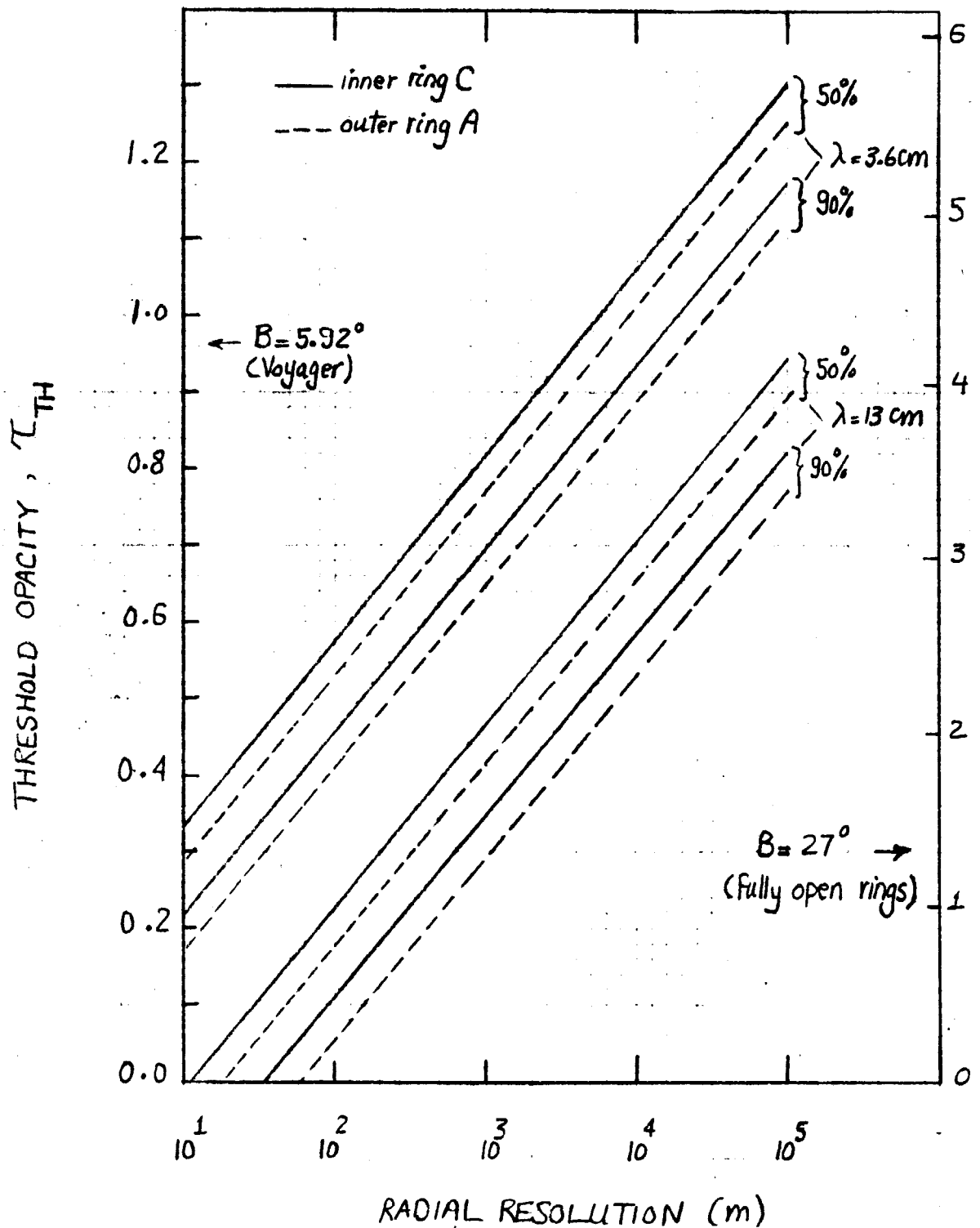


Fig. 6 Variation of Threshold Opacity with Radial Resolution.

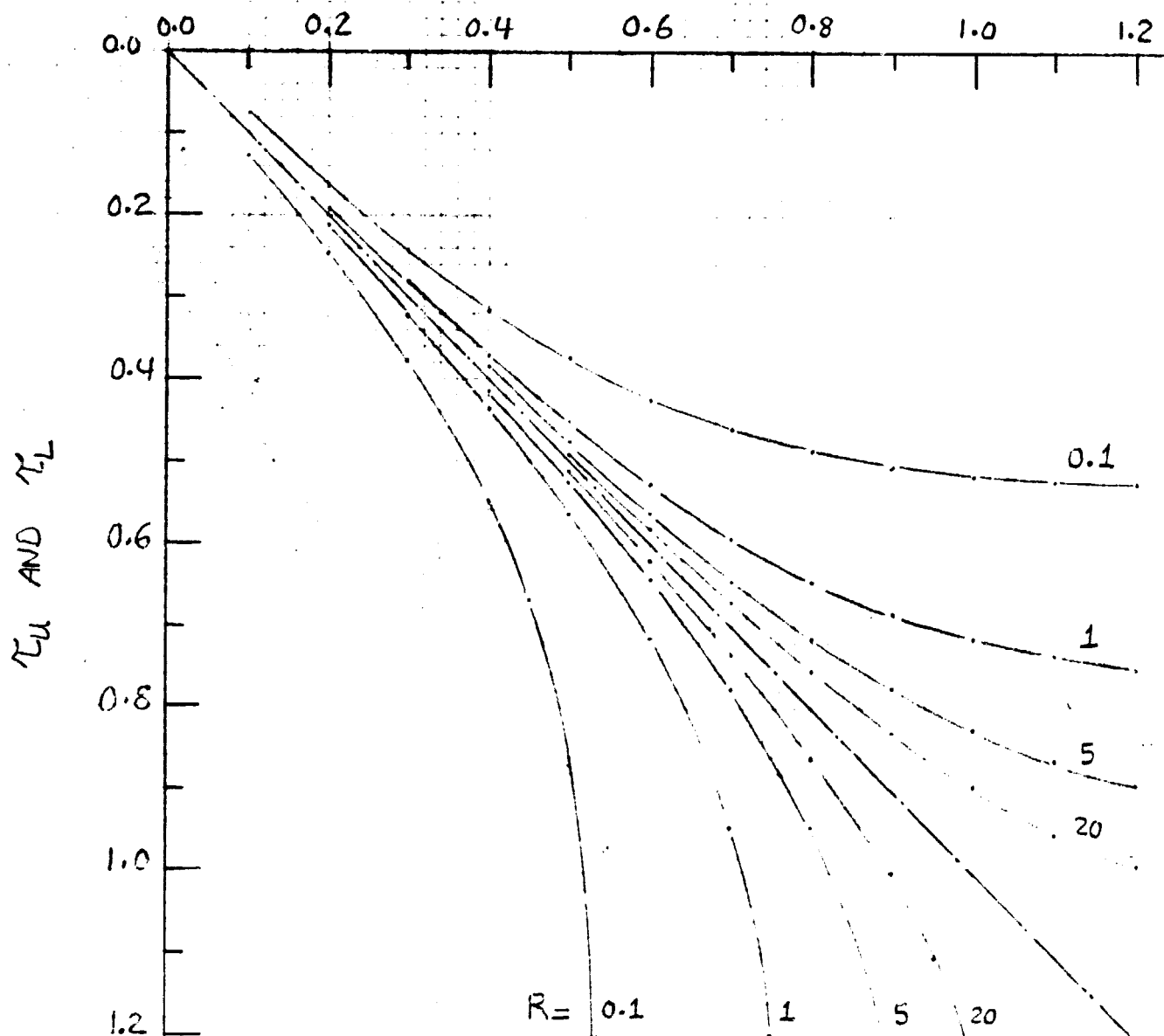
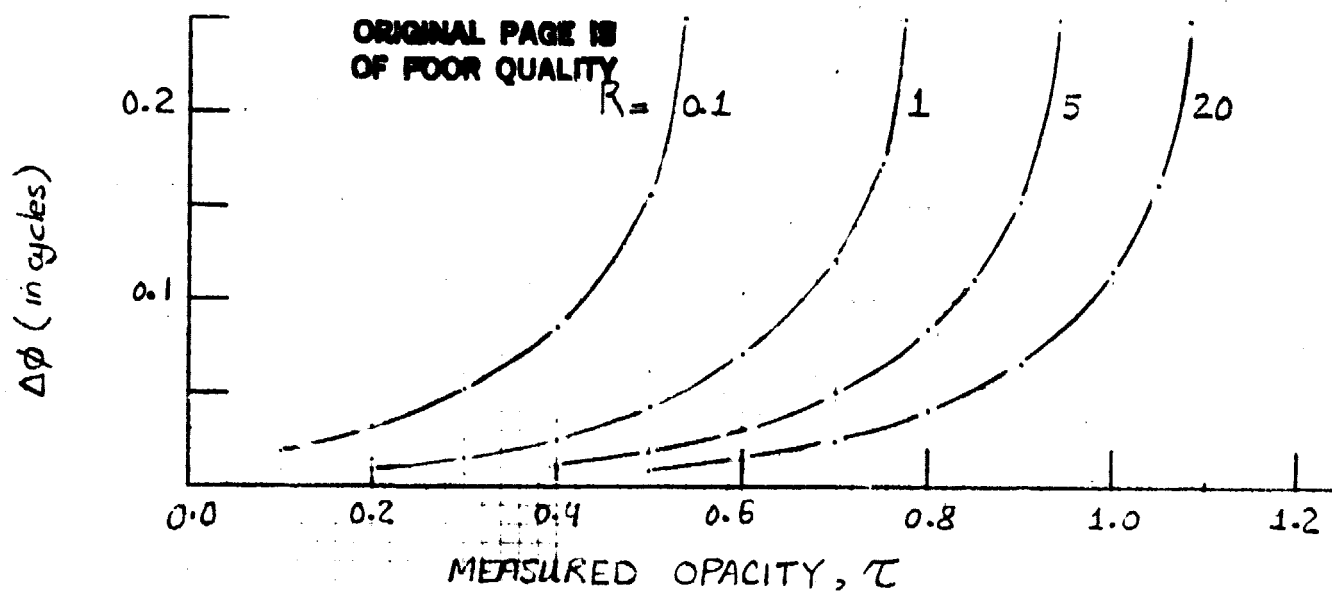


Fig 7. Variation of Uncertainty Intervals With Opacity and Resolution